# Application of historic datasets to understanding open solar flux and the 20th-century Grand Solar Maximum. 2. Solar observations

Article

Published Version

Lockwood, M. ORCID: https://orcid.org/0000-0002-7397-2172, Owens, M. J. ORCID: https://orcid.org/0000-0003-2061-2453, Yardley, S. L., Virtanen, I. O. I., Yeates, A. R. and Muñoz-Jaramillo, A. (2022) Application of historic datasets to understanding open solar flux and the 20th-century Grand Solar Maximum. 2. Solar observations. Frontiers in Astronomy and Space Sciences, 9. 976444. ISSN 2296-987X doi: 10.3389/fspas.2022.976444 Available at https://centaur.reading.ac.uk/106444/

To link to this article DOI: http://dx.doi.org/10.3389/fspas.2022.976444

Publisher: Frontiers

frontiers | Frontiers in Astronomy and Space Sciences

TYPE Review
PUBLISHED 07 September 2022
DOI 10.3389/fspas.2022.976444

Check for updates

OPEN ACCESS

EDITED BY
Dipankar Banerjee,
Indian Institute of Astrophysics, India

REVIEWED BY
Robert Cameron,
Max Planck Institute for Solar System Research, Germany
Susanta Kumar Bisoi,
National Institute of Technology Rourkela, India

*CORRESPONDENCE
Mike Lockwood,
m.lockwood@reading.ac.uk

SPECIALTY SECTION
This article was submitted to Stellar and Solar Physics,
a section of the journal
Frontiers in Astronomy and Space Sciences

RECEIVED 23 June 2022
ACCEPTED 11 August 2022
PUBLISHED 07 September 2022

CITATION
Lockwood M, Owens MJ, Yardley SL, Virtanen IOI, Yeates AR and Muñoz-Jaramillo A (2022), Application of historic datasets to understanding open solar flux and the 20th-century grand solar maximum. 2. Solar observations.
*Front. Astron. Space Sci.* 9:976444.
doi: 10.3389/fspas.2022.976444

# Application of historic datasets to understanding open solar flux and the 20th-century grand solar maximum. 2. Solar observations

Mike Lockwood[1]*, Mathew J. Owens[1], Stephanie L. Yardley[1,2,3], Iiro O. I. Virtanen[4], Anthony R. Yeates[5] and Andrés Muñoz-Jaramillo[6]

[1]Department of Meteorology, University of Reading, Reading, United Kingdom, [2]Donostia International Physics Center (DIPC), Donostia, Spain, [3]Mullard Space Science Laboratory, University College London, Dorking, United Kingdom, [4]Space Physics and Astronomy Research Unit, University of Oulu, Oulu, Finland, [5]Department of Mathematical Sciences, Durham University, Durham, United Kingdom, [6]Division of Space Science and Engineering, SouthWest Research Institute, Boulder, CO, United Kingdom

We study historic observations of solar activity from the 20th-century rise towards the peak of the Modern Grand Solar Maximum (MGSM) and compare with observations of the decline that has occurred since. The major difference in available solar observations of the rise and of the fall are accurate magnetograms from solar magnetographs: we here use synthetic magnetograms to interpret the rise and employ historic observations of Polar Crown Filaments to test them and verify their use. We show that eclipse images at sunspot minimum reveal the long-term variation of open flux deduced from geomagnetic observations in Paper 1 (Lockwood et al., 2022). We also make use of polar coronal hole fluxes derived from historic white light images of polar faculae, but have to consider the implications of the fact that these facular images do not tell us the polarity of the field. Given this caveat, the agreement between the polar coronal hole fluxes and the values derived from open flux continuity modelling based on sunspot numbers is extremely good. This comparison indicates that one possible solution to the "open flux problem" is open flux within the streamer belt that potential-based modelling of coronal fields from photospheric fields is not capturing. We take a detailed look at the solar cycle at the peak of the MGSM, cycle 19, and show the variation of the polar coronal hole fluxes and the inferred poleward flux surges are predictable from the asymmetries in flux emergence in the two hemispheres with implied transequatorial flux transfer and/or "anti-Hale" (or more general "rogue" active region flux) emergence late in the sunspot cycle.

KEYWORDS

**open solar flux, historic reconstructions, synthesized magnetograms, *in-situ* heliospheric measurements, polar faculae, crown filaments, eclipse observations**

## 1 Introduction

Modern solar physics can be traced back to December 1610 when Thomas Harriot recorded the first telescopic observations of sunspots in his notebooks (Vokhmyanin et al., 2020). It is likely that Galileo Galilei started making such observations about the same time but we have no records to confirm this. This was followed soon after by recorded observations by Christoph Scheiner and Johannes Fabricus in March 1611. The records of sunspots that we do have from Galileo start in 1612 and are of unprecedented quality (Vokhmyanin and Zolotova, 2018). The rapid spread and development of the telescope meant that by 1620 a considerable number of astronomers were making telescopic observations of sunspots across Europe (Vaquero and Vázquez, 2009).

The sunspot cycle was first suggested by Christian Horrebow in 1775, based on his observations over the previous 14 years (Jørgensen et al., 2019; Karoff et al., 2019) and firm evidence was published by Samuel Heinrich Schwabe in 1844, based on his observations that began 19 years earlier and which he continued until 1867, (Arlt, 2014). From these and other observations, Rudolf Wolf (1852) designated the first numbered solar cycle to have started in February 1755 and at the time of writing (2022) we are in the rising phase of cycle number 25. Lists of cycle start/end dates and cycle maximum dates are given at https://www.sidc.be/silso/cyclesminmax. The infrequent nature of observable eclipses meant that it was not immediately recognized that the nature of the solar corona varied over the solar cycle. First suggestions appear to be by Pierre Jules César Janssen in 1878, and by Arthur Cowper Ranyard (1879) in his survey of coronal forms published in Memoirs of the Royal Astronomical Society. Frank Bigelow (1890) was the first to recognise the solar magnetic field was the key component in the coronal structure. Eclipse observations showed that at sunspot minimum there was a well-defined belt of streamers at low heliographic latitudes separating two clear dark gaps (polar coronal holes), whereas at sunspot maximum streamers were found at all heliographic latitudes. (e.g. Waldmeier, 1977; Loucif and Koutchmy, 1989; Rušin, 2000; Sýkora et al., 2002; Pasachoff et al., 2009; Judge et al., 2010; Rušin et al., 2010; Tlatov, 2010; Boe et al., 2020). Coronal holes (Cranmer, 2009) are dark areas in the solar corona seen in extreme ultraviolet (EUV) and soft x-ray solar images, as well as using the *HeI* line at 1.083 $\mu m$ in the near infrared. They are dark because they are cooler, less dense regions than the surrounding plasma because they comprise "open" magnetic field lines that extend far into the heliosphere, along which the solar wind can escape more readily in the fast solar wind. The spatial distribution and area of coronal holes varies over the solar cycle (Simon, 1979; Cranmer, 2009; Hewins et al., 2020) with large polar coronal holes at sunspot minimum but also low-latitude coronal holes at all times. The latter can be separated into isolated coronal holes, which typically exist for several Carrington rotations, and transient coronal holes which last for between a few hours and about 2 days and are associated with transient events (Abramenko et al., 2010; Petrie and Haislmaier, 2013; Bilenko and Tavastsherna, 2016). In addition, the polar coronal holes in the declining phase of the cycle often show extensions to low latitudes, and even into the opposite solar hemisphere, and such events can last 10 or more Carrington Rotations (Bromage et al., 2000; Rouillard and Lockwood, 2007). Wang et al. (2010) used EUV images from the exceptionally long and low solar minimum between sunspot cycles 23 and 24 to show small coronal holes appear on the edges of newly-emerged active regions and then expand and becoming attached to the polar holes, consistent with modelled magnetic flux transport across the surface of the Sun and in the solar corona. This is discussed further in Section 7, which draws the important destinctions between photospheric flux circulation, coronal hole flux circulation and Open Solar Flux (OSF) circulation.

Paper 1 (Lockwood et al., 2022) studied the signed OSF, $F_S$ defined as the magnetic flux of one polarity (toward or away from the Sun) threading the coronal source surface. This surface is often taken to be spherical and at heliocentric distance $r = 2.5R_\odot$ (where a mean photospheric radius, $R_\odot = 6.96 \times 10^8 m$). Eclipse and coronagraph images show that the streamer belt extends beyond $r = 2.5R_\odot$ and so this definition of open flux includes both (signed) streamer belt open flux $F_{SB}$ and (signed) coronal hole open flux $F_{CH}$. The key difference between the two is the volume of the magnetic flux tube, which depends primarily on how far it extends into the heliosphere (or even beyond) and so on the time elapsed since it emerged through the coronal source surface. Paper 1 (Lockwood et al., 2022) detailed the quantification of the long-term variation in $F_S = F_{SB} + F_{CH}$, as determined from historical geomagnetic activity records. In this paper we look at historic solar observations and recent flux transport modelling that help us understand the observed long-term variation in OSF.

## 2 Eclipse observations

An episodic source of information on the state of the solar corona in the past is imagery of the Sun taken during total solar eclipses (Sýkora et al., 2003; Wang et al., 2007; Habbal and Druckmüller, 2019) and these have been used to study long-term change in the solar magnetic field (Owens et al., 2017a; Hayakawa et al., 2021; Lockwood and Owens, 2021).

The visible corona is split into two classes, the structureless F-corona, due to scattering of photospheric light by dust, and the magnetically structured K-corona due to Thompson scattering of light from the photosphere by electrons. At heliocentric distances $r$ exceeding about $2.5R_\odot$ the F-corona becomes brighter than the K-corona (e.g., Figure 1 of Reginald et al., 2017) and it becomes increasingly difficult for the human eye to discern the K-corona. However, as first noted by Ranyard (1871), this is overcome by instruments with polarization separation.

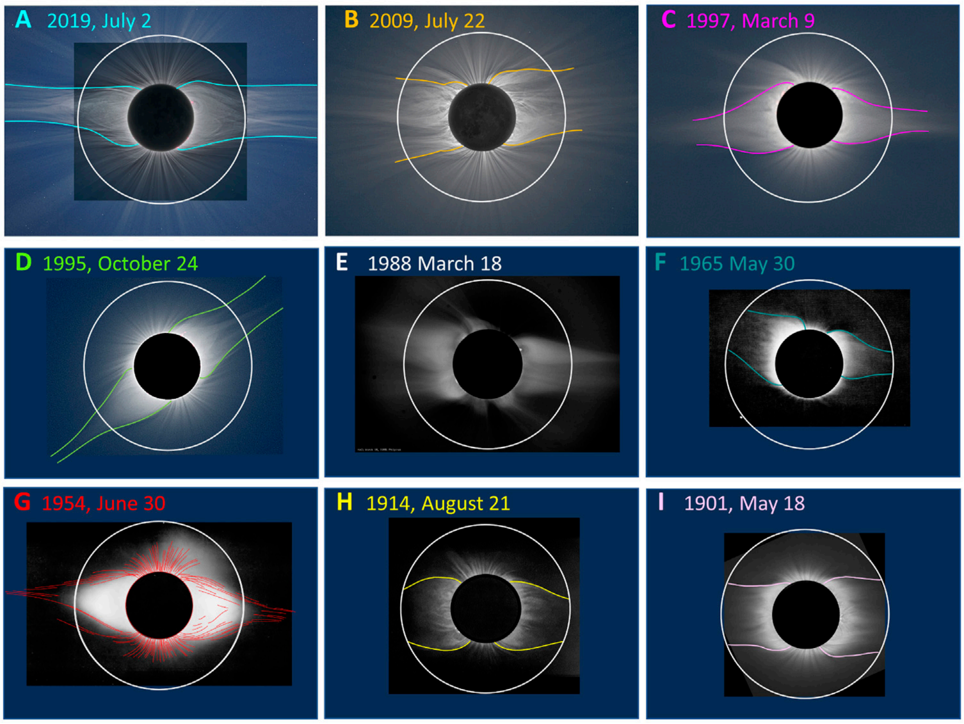

FIGURE 1
Photographic observations of total solar eclipses near sunspot minimum over the past 120 years. On each image has been added the nominal solar source surface at heliocentric distance $r = 2.5R_{\odot}$ and the estimated boundaries of the streamer belt on both the east and west limbs of the Sun. In each event, the heliocentric angular widths of the streamer belts, as seen from Earth, on the East and West limbs ($\Lambda_E$ and $\Lambda_W$, respectively) are then scaled from these estimated edges at $r = 2.5R_{\odot}$ and a mean streamer belt width computed $\Lambda_{SB} = (\Lambda_E + \Lambda_W)/2$. Events are: **(A)** 2 July 1991 (5 months before the sunspot minimum between cycles 24 and 25), image from Tres Cruses, Chile by Peter Aniol (PA), processed by Miloslav Druckmüller (MD) (Druckmüller et al., 2006); **(B)** 22 July 2009 (7 months after minimum 23/24), image from Enewetak Atoll, Marshall Islands by PA, MD, Vojtech Rušin (VR), Ľubomír Klocok, Karel Martišek, and Martin Dietzel, processed by MD; **(C)** 9 March 1997 (8 months after minimum 22/23), image from Yerofei Pavlovich, Siberia, Russia by Úpice observatory, processed by MD; **(D)** 24 October 1995 (10 months before minimum 22/23), image from Neem Ka Thana, Rajasthan, India by VR, processed by MD; **(E)** 18 March 1988 (18 months after minimum 21/22), image from the Philippines by the High Altitude Observatory; **(F)** 30 May 1965 (7 months after minimum 19/20) image from a NASA aircraft over Canada by Sturrock and Smith (1968) (see also sketch by Waldmeier (1966)); **(G)** 30 June 1954 (2 months after minimum 18/19) image from Syd Koster Island, Sweden, by Gold (1955) overlaid with sketch by Waldmeier (1955); **(H)** 21 August 1914 (14 months after minimum 14/15) image from Minsk, Russia by H.S. Jones and C.R. Davidson processed by A. Crommelin (Dyson, 1927); **(I)** 18 May 1901 (7 months before minimum 13/14) image from Pamplemousses, Mauritius by Edward Maunder and Annie Maunder, processed by William Henry Wesley (Dyson, 1927). For the last two events the image processing used was to make drawings from several large photographic plates. Note that the 18 March 1988 event **(E)** is the furthest removed from sunspot minimum and there is no clear distinction between a single streamer belt and two clear polar coronal holes: hence this event is not included in the survey of sunspot minimum events.

Figure 1 shows a series of images of eclipses taken near sunspot minimum over the past 120 years. The image **E** for the 18 March 1988 event is a long time (18 months) from the minimum between cycles 21 and 22 and, unlike the others shown, does not have a clear, definitive single streamer belt separated by clear polar coronal holes: it is an example of an image that is not included further in this study because it is too removed from sunspot minimum. The other images in Figure 1 demonstrate that the streamer belt around sunspot minimum is not constant in width. An estimate of the width of the streamer belt can be made by taking the difference, in heliographic latitude, of the edges of the streamer belt at a set value of $r$ (we here use the nominal coronal "source surface" at $r = 2.5R_{\odot}$). This is here done separately for the east and west limbs of the Sun and the two values averaged to give $\Lambda_{SB}$. However, defining the streamer belt edges is not straightforward. Wang et al. (1997) showed that the structure of the streamer belt observed at low sunspot activity years originates from a single tilted and warped plasma sheet centered around the neutral current sheet. When the edge-on parts of the plasma sheet rotate in and out of the plane of the sky, they produce arc-shaped features. Modelling can generate and predict eclipse images (Saez et al., 2005; Mikić et al., 2018), but inversion of this procedure and determining the width of the warped plasma sheet from images is complex (Boe et al., 2020). We have to consider that there are other difficulties that make such a detailed analysis excessive in the cases presented here. Most importantly there is longitudinal structure (warp) of the streamer belt so the northern edge on one limb of the Sun, as seen from Earth, may be set by plasma at a different Carrington longitude to that which sets the southern edge, thereby making the apparent latitudinal width greater than it should be. There are also structures in streamers (Wang et al., 2000) that make the streamer belt edge ambiguous and there are temporal changes that could mean what is seen depends on the precise timing of the image and the rotation of the Sun. Even images from different points along the path of totality of the same eclipse have been shown to reveal some differences due the temporal changes in the corona (Belík et al., 2006; Hanaoka et al., 2014). However, a limit to the uncertainties in determining an average streamer belt width is obtained from the time series of processed white light images from the LASCO coronagraph on SoHO, generated and studied by Lamy et al. (2014). These images are integrations over half a Carrington rotation after a number of corrections. The average streamer belt boundaries were defined from these LASCO images using a fixed level of derived coronal electron density rather than the subjective judgement based on emission intensity used with the eclipse images: although there is some variation from image to image of the mean latitude of the streamer belt, there is very little in the width, especially at sunspot minimum.

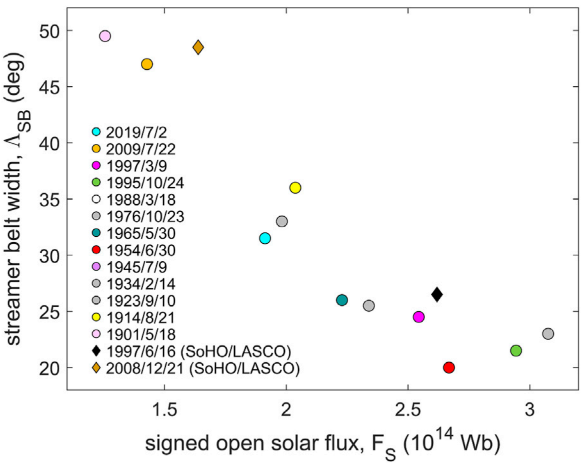

**FIGURE 2**
The variation of inferred streamer belt width $\Lambda_{SB}$ for observations within 1 yr of sunspot minimum, with the annual mean of the Open Solar Flux (OSF) derived from geomagnetic activity. The circles are for total solar eclipse estimates and the diamonds are two values derived from SoHO/LASCO coronagraph observations (Lamy et al., 2014).

Figure 2 shows that the sunspot-minimum streamer belt width derived from the images, $\Lambda_{SB}$, has an inverse relationship with the open solar flux (OSF), $F_S$ derived from geomagnetic activity and as presented in Paper 1 (Lockwood et al., 2022). This relationship is predicted by simple global flux-continuity modelling of both $\Lambda_{SB}$ and $F_S$ by Lockwood and Owens (2014). This modelling is based of the OSF-continuity concept by Solanki et al. (2000), namely that the rate of change of OSF is equal to its global production rate $S$ minus its global loss rate $L$. This concept has subsequently been used by many authors with refinements to the production and loss rate formulations used (Lockwood, 2003; Owens and Crooker, 2006; Owens and Crooker, 2007; Schwadron et al., 2010; Vieira and Solanki, 2010; Owens and Lockwood, 2012; Goelzer et al., 2013; Krivova et al., 2021). Lockwood and Owens (2014) used $S$ estimated from sunspot numbers based on the estimated open flux emergence in Coronal Mass Ejections (Owens and Crooker, 2006; Owens and Lockwood, 2012) and a theory-based loss rate $L$ that depends on the heliospheric current sheet tilt and hence the phase of the solar cycle (Owens et al., 2011; Owens and Lockwood, 2012). Lockwood and Owens (2014) subdivided the OSF (by definition the flux threading the coronal source surface) into streamer belt OSF and coronal hole OSF: they assumed all OSF emerged into the streamer belt and subsequently evolved into coronal hole flux over an extended distribution of timescales (between 0 and 5*yrs*) and thereby modelled the long-term variation of both the coronal hole flux $F_{CH}$ and the streamer belt flux $F_{SB}$ and hence the total OSF, $F_S$, and the streamer belt width $\Lambda_{SB}$. In the modelling the distribution of timescales for streamer-belt OSF evolving into coronal hole OSF was varied until the model reproduced the timings of the polar cap field reversals. However there is other evidence that supports the values used. The appearance and motion of OSF footpoints will be a convolution of the appearance and motion of photospheric flux and the time for that flux to evolve into coronal hole flux. Hewins et al. (2020) and Fujiki et al. (2016) use identification of coronal holes from EUV images with magnetograph data to track the formation and motion of coronal holes. The results on a super-synoptic map (latitude-time plot of longitudinal averages) show a butterfly pattern, very similar to that of sunspots, of shorter lived coronal holes associated with active regions. Secondly there are unexplained appearances of short-lived coronal holes which may be the effects of interchange reconnections. Thirdly there are coronal holes that migrate to the pole along the paths of the poleward moving photospheric footpoints, particularly of the trailing-spot polarity in the first surge toward the pole of each cycle. The number of these increase with distance along the path indicating the distribution of times after emergence through the photosphere in the butterfly wing that it takes these poleward moving flux tubes to become coronal holes and this supports the range of timescales between 0 and 5 yrs (with a mean of 2.5) used in the model. The same pattern is seen in the super-synoptic map of OSF from PFSS modelling (Wang, 2017) (see the next section).

The variation of derived $\Lambda_{SB}$ from the model, both over the solar cycle and with centennial-scale trends, agreed well with that derived from both modelling of the streamer belt based on magnetograph data and from observations of eclipses

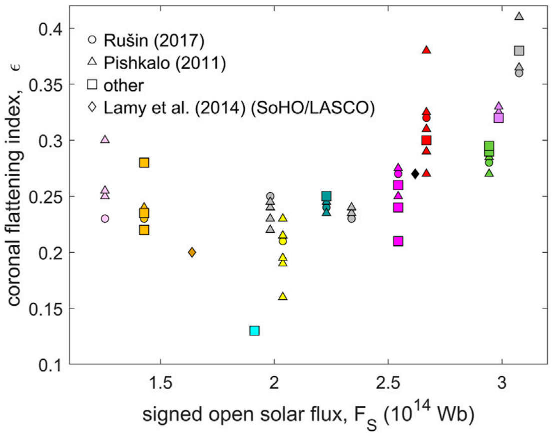

FIGURE 3
The variation of estimates of the coronal flattening index, $\epsilon$ with OSF derived from geomagnetic activity, $F_S$. The symbol shape gives the study that is the origin of the flattening index value and the color of the sybmols gives the date of the event, using the same color scheme as in Figure 2. The diamonds are two values derived from SoHO/LASCO coronagraph observations (Lamy et al., 2014).

(Lockwood and Owens, 2014; Owens et al., 2017a; Lockwood and Owens, 2021) and has been used to interpret eclipse observations in and immediately after the Maunder minimum by Hayakawa et al. (2021). The relationship at sunspot minimum shown in Figure 2 is expected because at sunspot minimum a big part of $F_S$ is the OSF in polar coronal holes, $F_{CH}$, and larger $F_{CH}$ means larger area of those polar coronal holes and so a smaller streamer belt width $\Lambda_{SB}$ (Makarov et al., 2003).

There are undoubtedly considerable uncertainties in the estimation of $\Lambda_{SB}$ from the eclipse images, which makes the agreement with the two points shown by diamonds in Figure 2 a useful confirmation. These two points are not taken from eclipse images but from the data from isophotes in integrated images recorded by the SoHO LASCO coronagraph by Lamy et al. (2014).

There have been other, more quantitive, analyses of the form of the corona in eclipse images, for example using isophotes to define the "coronal flattening" index, $\epsilon$. This has been generated for a number of eclipses by a variety of authors (Pishkalo, 2011; Marzouk et al., 2016; Priyatikanto, 2016; Rušin, 2017). The results from different studies of the same eclipse show some degree of agreement as well as some differences. Figure 3 shows the variation of $\epsilon$ estimates for sunspot minimum eclipses as a function of OSF. A larger $\epsilon$ means that the streamer belt width $\Lambda_{SB}$ is smaller and so there is general agreement between Figures 2 and 3 at $F_S > 1.5 \times 10^{14} Wb$. However, at lower $F_S$ the value of $\epsilon$ increases with decreasing $F_S$. This can be understood from the effect of $F_S$ and sunspot number on the intensity of the streamer belt corona (Lebecq et al., 1985) which occurs in addition to its effect on the coronal structure and the size of the polar coronal holes, the latter being the dominant effect at higher $F_S$.

Another way in which eclipse events have been used to study long-term variations of the corona is from observations by ionosondes of the decline in peak plasma density of the ionospheric E-layer during eclipse events, plasma that is generated by photoionization by solar EUV emissions. Minnis (1956) pointed out that off-disk EUV emission from the corona would still reach Earth during total solar eclipses and so influence the decline of E-layer ionospheric plasma densities seen. This off-disk coronal EUV emission varies with the sunspot number (Seaton et al., 2013). Davis et al. (2000), Davis et al. (2001), Davis et al. (2009) have shown that the off-disk coronal EUV emissions also show long-term variations by studying a series of measurements of the peak E-layer density during a series of eclipses dating back to 1932. Good agreement with the OSF variation is found once a number of corrections to allow for details of the measurement and method are deployed.

From the above, we conclude that the long-term variation of OSF deduced from geomagnetic activity, as reviewed in Paper 1 (Lockwood et al., 2022), is reflected in the sunspot-minimum structure of the solar corona as seen in eclipse events and (for recent minima) in images from the LASCO coronagraph on SoHO.

## 3 Observations and modelling of solar magnetic fields

In 1908 George Ellery Hale, working at Mount Wilson Observatory (MWO), introduced the application of the Zeeman effect to astrophysics by using it to remotely sense the magnetic fields in sunspots (Hale, 1908). These observations revealed Hale's polarity law and Joy's law (Hale et al., 1919), both forming fundamentals of understanding of the solar magnetic cycle and hence the sunspot cycle.

Half a century later, the Zeeman effect was again exploited in the photoelectric magnetograph by the son-and-father team of Horace and Harold Babcock (Babcock and Babcock, 1952; Babcock, 1953). Since then, magnetographs have been used routinely to map the weaker solar magnetic fields in the photosphere across the whole solar disk as well as the stronger magnetic fields in active regions. Photospheric magnetic field was routinely observed after 1953 (Babcock, 1961; Howard, 1972) but well-calibrated and stable observations only began with the advent of the Wilcox Solar Observatory (WSO) magnetograph in 1975. However, the WSO instrument has relatively low spatial resolution and suffers from saturation of strong fields. Higher resolution was provided by the NSO Kitt Peak (KP) instrument that also began routine operations in 1975 but several instrument updates make the data series less homogeneous than the WSO data series. Inter-calibration and combination of data from the WSO, MWO, KP and three other magnetographs was carried out by Virtanen and Mursula (2016), Virtanen and Mursula (2017), Virtanen and Mursula (2019). This is very important work which will continue into the future as more detail of the performance of each magnetograph is understood and implemented.

Based on observations of the magnetic fields in active regions and elsewhere on the solar surface (in particular the polarity rules for sunspots and the polarity flip of polar fields), Babcock (1961) proposed the basis of a cyclic solar dynamo, in which the poloidal magnetic field of a global dipole is wound up by differential rotation, now thought to happen in an "overshoot layer" at the base of convection zone. Loops of the resulting azimuthal field rise through the convection zone and emerge through the photosphere because of their magnetic bouyancy, thus forming sunspot groups containing bipolar magnetic regions (BMRs). The trailing spot of the pair is at higher latitudes because of the poloidal field component provided by the global dipole. This BMR "tilt" leads to a preferential cancellation of leading-polarity magnetic flux across the solar equator, leaving residual net trailing-polarity flux in each hemisphere (that polarity being opposite in the two hemispheres and reversing about 1 yr after the maximum of each solar cycle). This flux spreads over the hemispheres and migrates poleward under a meridional circulation, it eventually cancels and reverses the global dipole field in a series of reconnection events (see, for example Sun et al., 2015). The distribution of tilt angles has a key role in the development of the solar cycle (Dasi-Espuig et al., 2010). Leighton (1964) added radial shear to the differential rotation and treated the transport of surface magnetic flux by supergranular flows in terms of a diffusion model. Note that this Babcock-Leighton (B-L) model does not invoke the so-called "mean-field $\alpha$-effect", driven by the Coriolis force, that was invoked in the dynamo model of Parker (1955): this generates similar behaviour but is conceptually different and does have different consequences (Dikpati and Charbonneau, 1999; Hazra et al., 2020) especially for the solar cycle "memory" (Muñoz-Jaramillo et al., 2013).

These observations are all of magnetic fields in the photosphere. In the corona, the weaker magnetic fields and the higher temperatures mean that the Zeeman splitting is always small compared to the thermal line broadening and using the effect to determine magnetic field has only been possible in a few regions of very strong fields over active regions (Lin et al., 2004). Other approaches have been explored but, as yet, none have been successful enough to deploy in making routine measurements (Raouafi et al., 2016). Consequently, coronal magnetic fields are usually approximated using MHD modeling or extrapolation of photospheric measurements (Mackay and Yeates, 2012; Wiegelmann et al., 2014; Wiegelmann and Sakurai, 2021).

The simplest and most commonly-used method to extrapolate photospheric field into the corona has been the Potential Field Source Surface (PFSS) procedure (Altschuler and Newkirk, 1969; Schatten et al., 1969; Wang and Sheeley, 1992). This method has been deployed in a number of ways and is based on a large number of assumptions, the most crucial of which is that there is no electric current in the corona. This limitation is addressed by a combination of magnetic flux transport and magneto-frictional simulations, which can allow for currents below the coronal source surface (Yeates et al., 2010). Another approach is to use a global coronal MHD model, constrained by photospheric magnetic field observations made by a magnetograph (Riley et al., 2001; Riley et al., 2011).

## 4 Polar faculae

Polar faculae appear in white light images of the photosphere as bright points near the solar poles, usually at heliographic latitudes above about 65°. In contrast to active region faculae at lower latitudes, they are isolated, more point-like, less bright, randomly distributed and more frequent at sunspot minimum (Tlatov and Tlatova, 2020). They are visible in daily white-light observations made at the Mount Wilson Observatory (MWO) between 1906 and 1990 (Sheeley, 1991), or those recorded at the National Astronomical Observatory of Japan (NAOJ, Mitaka Observatory) from 1951 to 1991 (Li et al., 2002) and also in *CaIIK*-line spectroheliograms from the Kodaikanal Solar Observatory (KoSO) from 1940 to 1985 (Sivaraman, 2000). All faculae are related to very small patches of enhanced magnetic field and the fields of polar faculae are in the kilo-Gauss range. They usually have the polarity of the general polar magnetic field; however, the ambient Quiet Sun regions around polar faculae have weak field of the opposite polarity (Okunev and Kneer, 2004). Hence the polar coronal hole field at sunspot minimum appears to be predominantly associated with polar faculae.

A link between the number of polar faculae and the polar field at sunspot minimum was found by Neil Sheeley (see Sheeley (1991) and references therein) who showed there was a strong correlation between the numbers of polar faculae from the MWO observations and the WSO polar field measurements. Muñoz-Jaramillo et al. (2012) have calibrated and scaled the MWO facular observations in terms of the polar fluxes, obtained by integrating data over the polar coronal hole and the results are shown in Figure 4. To calibrate the polar facular data, daily values of the flux were obtained from the observations by the Michelson Doppler Imager (MDI) magnetograph on the SoHO satellite. This was done by assuming the polar fields are radial to allow conversion of the observed line-of-sight (l-o-s) field to the field magnitude. The surface area of each MDI pixel was computed allowing for the viewing geometry. The magnetic flux through each pixel was then integrated over all latitudes poleward of a nominal assumed value of 70°. The outer three pixels on the solar disk were neglected because of the large noise amplification by the l-o-s to radial field conversion. To allow for the fact that only

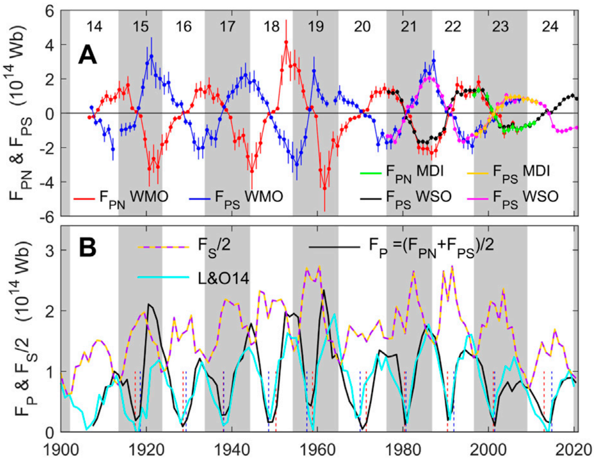

FIGURE 4
**(A)** Numbers of polar faculae from MWO images scaled by Muñoz-Jaramillo et al. (2012) in terms of polar magnetic flux using the fields measured by various magnetograph instruments. The red values are the derived polar flux for the northern hemisphere, $F_{PN}$ and the blue are for the southern hemisphere $F_{PS}$. The polarity is assumed to flip at each minimum value and the times of the corresponding polar field flips are shown by vertical dashed lines at the bottom of part **(B)** for after 1953 these are taken from magnetograms and before then from Kodaikanal observations (see text). The green and orange lines are the polar flux values derived from the Michelson Doppler Imager (MDI) magnetograph on the SoHO satellite for, respectively, the northern and southern hemisphere the and the black and mauve line are the corresponding values derived from the WSO magnetograph. **(B)** Comparison of the mean polar flux ($|F_{PN}| + |F_{PS}|$)/2 (black line) compared with $F_S/2$ (orange and mauve dashed line), where $F_S$ is the signed OSF and the factor 2 is discussed in the text. The cyan line is the coronal hole open flux, $F_{CH}$ from the continuity modelling of Lockwood and Owens (2014), (L&O14) updated to 2020.

part of the polar cap is visible at any one time the flux is then multiplied by the area of the full nominal polar cap (at $\Lambda > 70^\circ$) divided by the area of the usable MDI data that is integrated over. The MWO polar faculae numbers were then scaled in terms of the MDI polar fluxes by regression for the interval of overlap of the two. The error bars in Figure 4 are the computed uncertainties from each of these steps and the red and blue lines are the derived fluxes for the northern and southern polar coronal hole, $F_{PN}$ and $F_{PS}$, respectively. The WSO polar field data are scaled to a polar flux using the factor derived by Muñoz-Jaramillo et al. (2012) of $(1.06 \pm 0.06)\times 10^9 WbnT^{-1} = (1.06 \pm 0.06)\times 10^{18} m^2$. This comprises a scaling factor of 1.89 between the MDI and WSO field estimates (correlation coefficient 0.97) and an area factor of $2 \times 10^{18} m^2$, which corresponds to a polar cap poleward of a heliographic latitude of 70°. The latter factor is derived from a linear relationship between the polar field and the integrated flux from the MDI data (correlation coefficient 0.98).

The vertical dashed lines at the base of Part **B** of Figure 4 are the times of polar field polarity reversals (in red and blue for northern and southern hemisphere, respectively). These are determined from the WSO data for solar cycles 20–24 and the dates for cycle 19 were obtained from Babcock (1959) and Babcock (1961). For cycles 15–18 we use the dates derived by Mordvinov et al. (2020) from historic observations at the Kodaikanal Solar Observatory (KoSO) (see also Thomas et al., 2014). Mordvinov et al. (2020) estimate the polar magnetic field using the synoptic observations of the Sun's emission in the *CaIIK* and *Hα* spectral lines, using the fact that the *CaIIK* intensity correlates well with the unsigned magnetic flux, while the sign of the flux is derived from the corresponding *Hα* data that provides the information of the spatial maps of dominant field polarity because *Hα* filaments and filament channels mark out polarity inversion lines. The polar fluxes and their variation derived this way have similarities to those shown in Figure 4B, but there are differences. For example, the amplitude of the peaks at each sunspot minimum are similar but, in particular, the large peak at the minimum between cycles 18 and 19 derived from the MWO polar faculae is not observed. However, we note that the $A(t)$ index of Makarov et al. (2001) does show similar variations in the amplitude of sunspot cycle peaks, including that for solar minimum 18/19. The $A(t)$ index is the sum of the intensities of dipole and octupole components of the solar field inferred from *Hα* synoptic charts (and, in particular, the position of neutral lines indicated by filaments) for 1915–1999 that are interpreted by comparison with the WSO magnetic field observations for 1975–1999. In addition, the MWO polar field agree quite well with the polar network index (*PNI*) developed by Priyal et al. (2014) from chromospheric networks seen in Kodaikanal *CaIIK* spectroheliograms. Comparisons of the variations of $A(t)$, *PNI* and the polar field derived from the MWO polar faculae data have been presented in Figure 1 of Hazra and Choudhuri (2019). The agreement is generally good but in both cases there are cycles where not all three agree on the amplitude of the sunspot-minimum peak. Significantly, in none of the cycles do both *PNI* and $A(t)$ serously disagree with the variation derived from MWO polar faculae. Figure 11 of Petrovay (2020) compares the fields derived from MWO images with the numbers of polar faculae observed at NAOJ over the interval 1951 to 1991 (Li et al., 2002), and again there are strong similarities but there are also some differences.

Part **B** of Figure 4 compares the mean of the moduli of the polar fluxes shown in Figure 4A, ($|F_{PN}| + |F_{PS}|$)/2 with $F_S/2$, where $F_S$ is the signed OSF, presented and discussed in Paper 1 (Lockwood et al., 2022). If all OSF was gathered into the polar coronal holes at sunspot minimum, we would expect the agreement to be good between the average polar coronal hole flux and $F_S$ at such times. In fact, we find very good agreement at each minimum with $F_S/2$. Note this factor of two is not explained by signed and unsigned fluxes as $F_{PN}$, $F_{PS}$ and $F_S$ are all defined as signed. Figure 4B shows that there is excellent agreement between the cycle-to-cycle variations of ($|F_{PN}| + |F_{PS}|$)/2 and $F_S/2$ at the sunspot minima. An explanation of the factor 2 is provided by the modelling of Lockwood and Owens (2014), shown by the cyan line which is their modelled coronal hole OSF

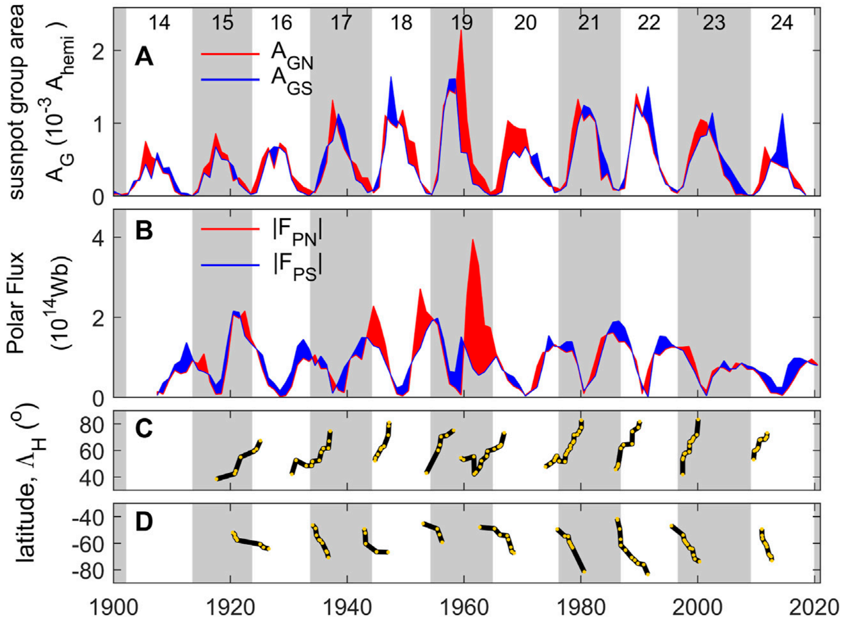

FIGURE 5
**(A)** Hemispheric sunspot group areas compiled and intercalibrated by Mandal et al. (2020). Red is for the norther hemisphere area $A_{GN}$ and blue for the southern, $A_{GS}$ and shaded areas show the difference between the two, coloured according to the larger of the two. **(B)** The polar fluxes derived from polar faculae, $F_{PN}$ and $F_{PS}$, as discussed in the previous section, and shown using the same format as **(A)**. **(C)** Observations of the polewardmost PCF found by Xu et al. (2021) in the northern hemisphere: observed heliographic latitudes are shown by yellow points, which are connected by a black line. **(D)** Same as part **(C)** for the southern hemisphere.

$F_{CH}$ from the model fit to the OSF derived from geomagnetic data $F_S$. It has been updated to 2020 and uses a slightly increased mean time constant for the transfer of streamer belt OSF to coronal hole OSF of 2.5 years, with a distribution of values between 0 and 5 years. As discussed in the previous section, this distribution of time constants and was obtained by iteration to make minima in $F_{CH}$ occur at the times of the polar field flips and the amplitude of the peaks at each sunspot minimum was not fitted in any way. It can be seen that the agreement with the polar coronal hole flux derived by Muñoz-Jaramillo et al. (2012) is excellent. The one exception to this is for the minimum between cycles 15 and 16 for which the polar flux peak from the MWO facular images is considerably larger than the estimated $F_{CH}$. It is difficult to attribute this to errors in the MWO data as this peak is similar (if slightly smaller) in the *PNI* data, although the $A(t)$ data do agree with the modelled $F_{CH}$ (see Figure 1 of Hazra and Choudhuri, 2019). The modelled values are showing that at each sunspot minimum only half the OSF is in polar coronal holes, the other half being within the streamer belt (i.e at sunspot minima $F_{CH} \approx F_{SB} \approx F_S/2$). PFSS modelling shows this fraction of OSF outside the polar coronal holes is not unreasonable (see Figure 5 of Koskela et al., 2019) but the total OSF derived is too small by roughly the factor two compared to the *in-situ* data (the open flux problem), even though the temporal variations are very similar (see Figure 8 Koskela et al., 2019).

It has been known for some time that low-latitude coronal holes persist at sunspot minimum (Levine, 1982; Luhmann et al., 2002; Abramenko et al., 2010; Hewins et al., 2020), what is perhaps surprising is that we here infer that they contribute as much OSF as the polar coronal holes. Potentially, this provides an explanation of the factor two difference between *in-situ* OSF values and those from photospheric modelling (Lockwood et al., 2022). One reason why much of this streamer belt OSF has been missed in PFSS modelling of the corona (at all phases of the solar cycle) is likely to be the assumption that the corona is current-free, an assumption that is directly contradicted by the fact that magnetic reconnection is commonly observed in the corona (see review by Pontin and Priest, 2022). Additional open flux in non-potential models arises through inflation of the magnetic field by coronal electric currents. Some additional fluctuations due to coronal mass ejections (CMEs) may be present, but these models can generate CME-like events. Open flux within the streamer belt has been seen in low-latitude coronal holes and near active regions. In addition, Wang and Sheeley (2004) and Fisk and Zurbuchen (2006) argue that “interchange reconnections”, often with flux in active regions, will introduce OSF, not necessarily with coronal hole signatures, into the streamer belt, although we note that modelling by Linker et al. (2011) suggests it is rapidly lost. The possibility of OSF in the streamer belt without coronal hole signatures could be an important consideration because integrating magnetic flux from global MHD modelling of the corona from magnetogram data over areas defined from EUV images to be coronal holes also gives a flux that is about 50% of the OSF derived from *in-situ* and geomagnetic data (the "open flux problem", see Paper 1) (Wallace et al., 2019; Linker et al., 2021).

Magnetohydrostatic (MHS) models describe the balance between the Lorentz force, plasma pressure, and gravitational forces in the corona. Large-scale plasma flows are neglected so the system can be considered stationary and the corona evolves only over timescales that are long, giving a series of dynamic equilibria. To simplify solution of the equations, the coronal electric currents are only field-aligned and perpendicular to gravity (Low, 1991). Koskela et al. (2019) show that increasing a fit parameter $a$ from 0.01 to 1.0, introduced to allow for the radial length scale of the coronal currents (Mackay and Yeates, 2012), increases the total OSF predicted by magnetostatic equivalents of PFSS by 50% at all phases of the solar cycle. The magneto-frictional non-potential modelling by Yeates et al. (2010) increased the OSF at solar minimum by only 25% and by 75–85% at solar maximum. Hence coronal currents appear to be part of the discrepancy, but do not appear to be the full solution. One major factor is the effect of transient events like coronal mass ejections. The model of Yeates et al. (2010) includes open flux coming from CMEs, because it generates flux rope eruption events. Recently, Bhowmik and Yeates (2022) have looked at the open flux evolution in the magnetofrictional model and shown that, in addition to flux rope eruptions, a lot of the smaller peaks in open flux come from "overlying arcade eruptions", where magnetic energy is released from higher in the coronal arcades These events have been seen before in MHD simulations of streamers and may correspond to observed "streamer blowouts".

Recent work by Rice and Yeates (2021) points to another factor. These authors describe an improved coronal magnetic field model that calculates a magnetofrictional equilibrium with an imposed solar wind profile. They find that this modelling can predict greater open flux, and more accurate values than are obtained for potential fields, especially for high outflow speeds, but there is a concern that this also leads to unrealistic streamer shapes. With a reasonable outflow speed of 150 $kms^{-1}$, about 30–40% of the discrepancy in open flux between solar and *in-situ* data is accounted for. Hence it is probably that the open flux problem has a number of solutions including these effects of outflow speed (Rice and Yeates, 2021), low-coronal currents (Yeates et al., 2010), episodic bursty enhancement from eruptions (Bhowmik and Yeates, 2022) and improved allowance for folded flux (a.k.a. field switchbacks) in the heliosphere (see the review of "excess flux" in Paper 1 Lockwood et al., 2022).

## 5 Polar crown filaments

Filaments are persistent features of the lower solar corona that are typically 100 times denser and 100 times cooler than the surrounding coronal plasma. When seen on the solar limb, usually in *Hα* emissions, they are called prominences whereas, filaments are the same phenomenon seen on the solar disk in absorption of *Hα* or *CaIIK* spectral lines. During periods of high sunspot activity, filaments are found broadly spaced from equatorial to polar latitudes (Mackay, 2021). Polar Crown Filaments (PCFs) are one of three classes of filament that form above magnetic polarity inversion lines which separate the old magnetic flux of the previous solar cycle and the new magnetic flux of the current cycle (Diercke and Denker, 2019). The occurrence and behaviour of PCFs varies over the solar cycle and from cycle to cycle, indicating that they hold information that is valuable to understanding the long term and solar cycle variation of the solar magnetic field (Webb et al., 2018; Xu et al., 2018; Emery et al., 2021), as proposed by McIntosh (1972). In particular, Hyder (1965) noted that the poleward migration of PCFs was associated with the flips of the polar magnetic field near the maximum of sunspot cycle 19, a feature that has been repeated in subsequent solar cycles.

Xu et al. (2018) and Emery et al. (2021) have surveyed the poleward motion of the polewardmost PCF using full-disk *Hα* images obtained from the Kodaikanal Solar Observatory, Kanzelhöhe Solar Observatory, and Big Bear Solar Observatory. These data cover the interval 1915–2020 and show that the poleward migration speed of the polewardmost PCF is generally greater in the northern solar hemisphere and northern-hemisphere PCFs reach their highest latitudes before those in the southern in most solar cycles. The migration speed of PCFs does not seem to be well correlated with the amplitude of the sunspot cycle.

Figure 5 shows the evolution of the heliographic latitudes of the polewardmost PCF in the north and south hemispheres (parts **C** and **D**, respectively) and compares with the observed hemispheric areas of sunspot groups compiled by Mandal et al. (2020) (part **A**) and the polar cap fluxes derived from MWO white light images (part **B**) (Muñoz-Jaramillo et al., 2012). Note that the variation of sunspot group area is very similar to the composites of plage area measurements (faculae observed in the chromosphere) compiled by Chatzistergos et al. (2020). The most asymmetric cycle in terms of both sunspot group areas and polar fluxes is cycle 19, in which both are dominated by the northern hemisphere. Figure 5C shows this cycle is also anomalous in the poleward migration of the PCFs in this hemisphere, being the only one not showing a monotonic progression towards the pole.

A commonly-used format of magnetogram, displaying the data from one or more magnetograph instrument, is a super-synoptic map—a plot of the average radial heliospheric field on a heliographic latitude ($\Lambda_H$)—time axis. Figure 6B is an example from the KP and SOLIS photospheric magnetic field observations from January 1978 (Carrington Rotation 1664) to December 2016 (CR 2184). Superposed on this magnetogram are the PCF locations shown in Figure 5. It can be seen that the polewardmost PCF does indeed chart the migration of the polarity reversal to

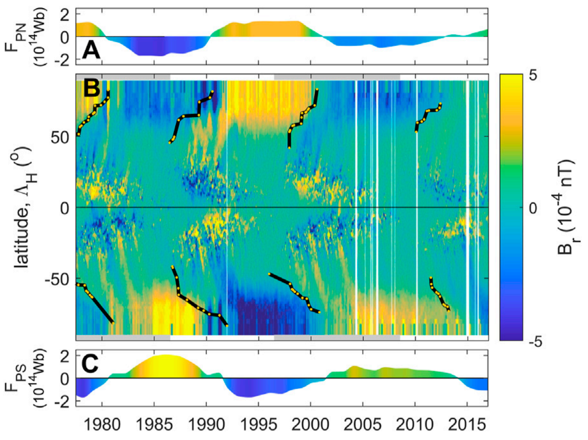

FIGURE 6
**(B)** Combined, intecalibrated magnetogram from the KP and SOLIS magnetograph instruments (see Virtanen and Mursula, 2016), Virtanen and Mursula (2017), Virtanen and Mursula (2019).Yellow and blue colors correspond to positive and negative polarity. White vertical lines are periods with no observations (from Virtanen et al., 2018). Superposed are the polar crown filament locations reported by Xu et al. (2018); Xu et al. (2021), as shown in 5. **(A,C)** show polar fluxes $F_{PN}$ and $F_{PS}$, respectively, from WSO polar field values scaled using the factor derived from field and polar faculae data measurements by the MDI instrument on SoHO (see Figure 4 and text for details).

the pole, caused by the first poleward surge of the cycle in that hemisphere of magnetic flux of the trailing-polarity field. This association has been reviewed by Cliver (2014) and here is shown for the PCF observations from various sources compiled by Xu et al. (2018), the same as used below for the time before accurate magnetograph data are available. An example of a strong surge was observed in cycle 24 and its causes were investigated using a flux transport model by Yeates et al. (2015) and its implications for OSF is the heliosphere were investigated by Lockwood et al. (2017).

## 6 Synthesized magnetograms

An important goal in reconstructing the past behaviour of the solar magnetic field is generating synthetic magnetograms from historic observations made before accurate magnetograph data became available. These synthetic magnetograms are valuable in many ways, for example in reconstructing solar irradiances (Dasi-Espuig et al., 2016; Wang and Lean, 2021) and for understanding solar magnetic flux circulation (Virtanen et al., 2019a).

The general principle is to describe the spatial distributions of the two emerged field polarities in the active region belts and then track the motion of the emerged field under the influences of differential rotation, meridional flow and supergranular diffusion. Initially the first stage was done using Bipolar Magnetic Regions (BMRs) and it was shown that the results depended critically on the tilt angles of the line connecting the centres of the two patches of oppositely-directed photospheric field in the BMR (Cameron et al., 2010). Observations made over recent solar cycles show that about 8% of all BMRs are of "anti-Hale" polarity (McClintock et al., 2014; Li, 2018; Muñoz-Jaramillo et al., 2021) and these have been dealt with statistically using a distribution of tilt angles which could depend on the amplitude of the cycle in question. More generally, the key factors that determine flux evolution are the latitudinal profile of photospheric rotation velocity and the latitudinal separation of BMR footpoints: Petrovay and Nagy (2018), point out this depends on tilt angle, $\alpha$ and the spatial separation, $d_{BMR}$ of the footpoints, as well as the BMR colatitude, $\theta_{BMR}$ and flux $F_{BMR}$. Hence anti-Hale BMRs are extreme examples of "rogue" active regions (Nagy et al., 2017; Nagy et al., 2019) which differ in the net effect of the factors $\alpha$, $d_{BMR}$, $\theta_{BMR}$ and $F_{BMR}$. There are concerns that the permutations of combinations of these parameters means that tilt angle does not specify the pattern of emerged flux sufficiently and, indeed, if BMRs are a reliable quantum unit of emergence with which to specify the distributions (Yeates, 2020).

Figure 7 shows synthesised magnetograms in super-synoptic map format that have been generated from a long series of operations to intercalibrate, process and test the synthesised data, described in full in a series of 7 papers (Pevtsov et al., 2016; Virtanen et al., 2017; Virtanen et al., 2018; Virtanen et al., 2019a; Pevtsov et al., 2019a; Virtanen et al., 2019b; Virtanen et al., 2021). The basis of the method is to reconstruct active regions from properly-calibrated historic *CaIIK* line synoptic maps and assign to them magnetic polarities using the historic sunspot magnetic field observations. The reconstructed active regions act as the input in a surface flux transport model of Yeates et al. (2015) to produce synoptic maps of the photospheric magnetic field. Hence Figure 7 has been reconstructed from observations from the time in question and not from the statistics of recent observations. Tests of the reconstruction technique against modern magnetograph data (Virtanen et al., 2019a) show that it very accurately reproduces the long-term evolution of the large-scale field, including the poleward flux surges and the strength of polar fields. Some weaker active regions are found to be missing, but these have only a very minor influence on the large-scale evolution of the field. There is, naturally, some uncertainty in the simulation; however, the tests show how far the techniques have developed towards making credible and reliable synthesised magnetograms from historic data. Figure 7B reveals that the synthesised magnetograms are reproducing with considerable accuracy the migration toward the pole revealed by the historic observations of the PCFs. Some features are remarkably well modelled, for example the brief and unique equatorward retreat of the PCFs in the northern hemisphere in 1962 can be seen to be caused by a prolonged

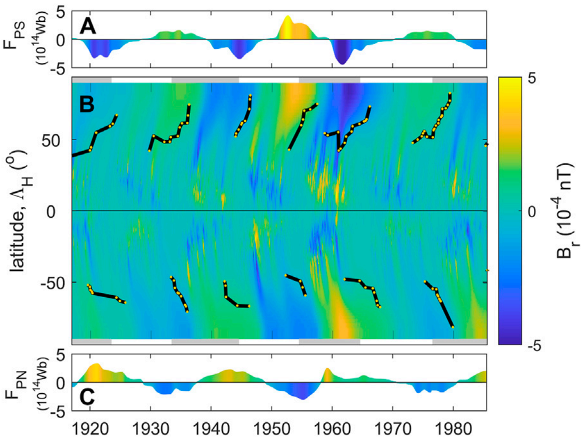

FIGURE 7
The same as Figure 6 but for synthesized magnetograms for 1915–1990. The polar fluxes shown in the top and bottom panels are the deduced from polar faculae from the MWO white light images.

poleward motion of the "wrong" polarity field ($B_r > 0$, in yellow/green, i.e. that of the leading sunspots) that was then followed by a surge of the "normal" polarity field ($B_r < 0$, in blue, i.e. that of the trailing sunspots).

There is also good general agreement with the polar fluxes $F_{PN}$ and $F_{PS}$ shown in the top and bottom panels (parts **A** and **C**, respectively) of Figure 7. In general, the effect of major surges of flux transport is well reflected in the polar faculae data; however, there are some differences. For example, in the Northern hemisphere, the strong increase seen in $F_{PN}$ from the MWO data in cycle 19 (peaking in 1952), which is earlier than predicted as is that in cycle 20 (peaking in 1961). In addition, the observed peak in 1920 is more pronounced than predicted in cycle 15, as it is when compared to the modelling of Lockwood and Owens (2014) (see Figure 4B). Some of these differences are discussed further in the next section.

## 7 Discussion and conclusion

The synthesized magnetograms shown in Figure 7 confirm the broad predictions made previously by Mordvinov et al. (2020) but give greater detail. Indeed the detail is now good enough for a plausible analysis of the causes and effects of individual poleward surges, of the kind carried out for actual magnetograph data (Lockwood et al., 2017; Mordvinov and Kitchatinov, 2019; Mordvinov et al., 2021).

There are a great many features in these combined datasets that we could discuss at length, but here just choose one, namely the peak of the Modern Grand Solar Maximum (MGSM) defined in Paper 1 (Lockwood et al., 2022). This was before the period of well-calibrated magnetograph observations and so the synthesized magnetograms and the historic observations are crucial. However, we do have some very early magnetograph data from the Hale Solar Observatory (HSO) and the Mount Wilson Observatory (MWO) which are not of sufficient accuracy or resolution for many purposes but nevertheless can provide some useful comparisons and constraints.

This peak of the MGSM is of particular interest because it, self-evidently, marks a turning point between the upward trend in solar activity of the early 20th century and the subsequent fall. Figure 4 shows that the peak amplitude of each solar cycle in OSF is strongly related to the value at the prior minimum, a relationship that is well known for sunspot numbers and sunspot group areas (Muñoz-Jaramillo et al., 2013). Figure 4B shows that the rise in the MGSM took place over solar cycles 14–19 with a "virtuous circle" (for OSF growth) based on two relationships: 1) the OSF at the peak of a cycle is determined by the polar coronal hole flux, $(F_{PN} + F_{PS})/2$), (and so the OSF) at the previous minimum and 2) the polar coronal hole flux at the end of the cycle (and so at the start of the next) is set by the previous peak in OSF. Figure 4B shows that relationship 1) continued to hold for cycle 19 and it was relationship 2) that broke down and led to the turning point. The subsequent cycle (cycle number 20) was anomalous in many ways and normal cycles were not re-established until cycle 21. For this and subsequent cycles both relationship 1) and 2) have again held, but this time with the "vicious circle" (for OSF growth) that gives the long-term decline. It therefore is of interest to take a close look at cycle 19 to see why relationship 2) broke down and such large OSF emergence did not result in a correspondingly large polar coronal hole flux by the end of the cycle.

### 7.1 Cycle 19: The peak of the MGSM

Waldmeier (1971) noted that the interval that we now know is the peak of the MGSM was a period of pronounced and long-lived north-south asymmetry in sunspot activity. Figure 5A shows that sunspot activity from the peak of cycle 19 to the peak of cycle 20 was significantly greater in the northern hemisphere. This is unusual as most recent cycles show a slight excess in the northern hemisphere in the rising phase and a slight excess in the declining phase in the southern hemisphere. In the rise up toward the MGSM peak, this was possibly the other way round, but differences were again small. The excess of northern hemisphere spots led to a major excess of polar flux in the northern hemisphere in the declining phase of cycle 19, at least as inferred from the MWO polar faculae observations (Figure 5B). However, by the end of cycle 19 that asymmetry had gone. Hemispheric asymmetry is of significance. It has been noted in many papers that sunspot activity was almost exclusively in the southern solar hemisphere during the last grand solar minimum, the Maunder minimum (e.g. Schüssler and Cameron, 2018; Hayakawa et al., 2021).

Asymmetry in active region emergence has also been linked to the period of Rieger-type oscillations (between about 160 and 190 days) seen in sunspot and other data. These are thought to be caused by magnetic Rossby waves in the dynamo overshoot layer near the tachocline and have been used to estimate magnetic field strengths there. These estimates are of order 45–49 *kG* in more active hemispheres (north during much of cycles 19 and 20) and 33–40 *kG* in weaker hemispheres (Gurgenashvili et al., 2017). Because the north-south asymmetry is most marked at the peak of the MGSM, explaining how it arises in the solar dynamo is likely to be key in understanding the MGSM.

Given how marked the north-south asymmetry of sunspots was around the peak of the MGSM, it seems very likely that the turning of rising solar activity to the subsequent fall is related to that strong asymmetry. However, we cannot say this with certainty because we have just one example of a grand maximum peak when we have simultaneous sunspot position data. Routine measurements of north-south asymmetry in sunspot numbers start in 1874 with the commencement of the Royal Greeenwich Observatory observations (Mandal et al., 2020). However, a number of recent studies of the notebooks of earlier sunspot observers have generated intervals for which the butterfly diagram (and hence any north-south asymmetry) can be derived for example for Schwabe's observations of 1825–1867 (Arlt et al., 2013), Horrebow's of 1767–1778 and Staudacher's of 1760–1780 (Karoff et al., 2019), Hevelius' of 1642–1645 (Carrasco et al., 2019) and Scheiner's of 1621–1631 (Arlt et al., 2016). None of these intervals show asymmetry as marked as that during the MGSM or as complete as that during the Maunder minimum, but neither do they show a major turning point in the trend of solar activity. There is a hint in the results from Scheiner that the southern hemisphere is starting to dominate 20 years ahead of the start of the Maunder minimum; however, the brief interval recorded by Hevelius a decade later shows no sign of this. Yet the solar cycles and long term indicators such as cosmogenic isotope fluxes show a gradual descent into the Maunder minimum at this time (Lockwood et al., 2011). The data from Meudon show that in the second half of the Maunder minimum spots were exclusively in the southern hemisphere and that the end of the minimum has heralded by just three spots reported in the northern hemisphere between 1704 and 1708 before a full and near-symmetric cycle was re-established (Hayakawa et al., 2021). Hence although it is clear that extreme hemispheric asymmetry was a key part in maintaining the Maunder minimum, the data we have give us almost no clues as to what role it played in generating the minimum.

Das et al. (2022) analysed sunspot position data since 1874 and concluded that the hemispheric asymmetry is largely governed by stochastic noise. The origin of the stochastic changes is debated, for example, it has been proposed to be rouge active regions (Nagy et al., 2019) or changes in meridional circulation (Hathaway and Upton, 2016). However, Das et al. (2022) also found that the time series is not completely determined by a memory-less stochastic noise and that there is a long-term persistence, which can go beyond two solar cycles. Other authors have identified this persistence in asymmetry when integrated over a solar cycle (Li et al., 2001; Leussu et al., 2016). In this context of possible longer-term memory we note that Bhowmik (2019) found from observations that asymmetry in polar fluxes at sunspot minimum was reflected in sunspot asymmetry in the subsequent cycle. The paradox of random fluctuations generating long-term trends in sunspot asymmetry was modelled by Nepomnyashchikh et al. (2019) who used random perturbations to tilt angle and yet generated trends that lasted several solar cycles.

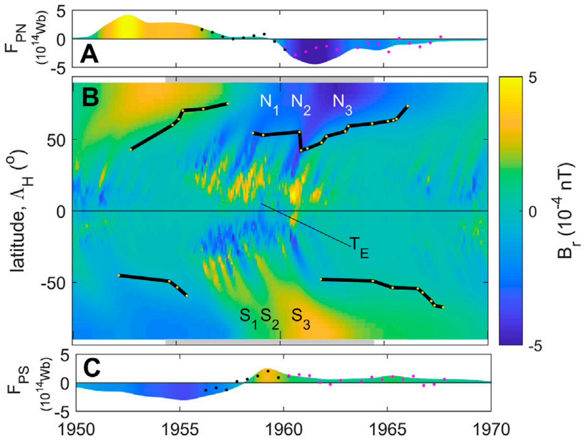

FIGURE 8
Detail of Figure 7 for solar cycle 19 at the peak of the Modern Grand Solar Maximum. In part **(B)** $N_1$, $N_2$ and $N_3$ are three poleward surge features of flux transport in the northern hemisphere and $S_1$, $S_2$ and $S_3$ are the corresponding features of poleward flux transport in the southern hemisphere. The feature labelled $T_E$ appears to show transequatorial transfer of toward polarity ($B_r < 0$) flux. In the top and bottom panels **(A,C)**, the coloured variations are the polar fluxes from MWO images of polar faculae, black dots show the 6-months averages of the polar field measured by the Hale Solar Observatory (HSO) magnetograph (from Babcock, 1959) and the mauve dots are 6-months averages of the polar field measured by the first magnetograph at Mount Wilson Observatory (MWO) (from Howard, 1972). In both cases, the polar fields have been scaled to the polar cap fluxes $F_{PN}$ and $F_{PS}$ using a scaling factor of $4 \times 10^{18}$ $Wb\ nT^{-1}$. The gray portions of the bars at the top and bottom of Part **(B)** denote sunspot cycle 19.

The Babcock-Leighton circulation means that it is field of the polarity of trailing spots migrating poleward in the rising phase of the solar cycle that flips the polar field polarity about a year after sunspot maximum. Frequently, however, there are brief intervals of predominantly leading-spot polarity field migrating poleward (Mordvinov and Kitchatinov, 2019). Indeed it is these intervals that allow us to see the poleward motion of flux on super-synoptic maps; the polarity changes giving the striations in the magnetograms, both observed and synthesized (Figures 6B, 7B, respectively).

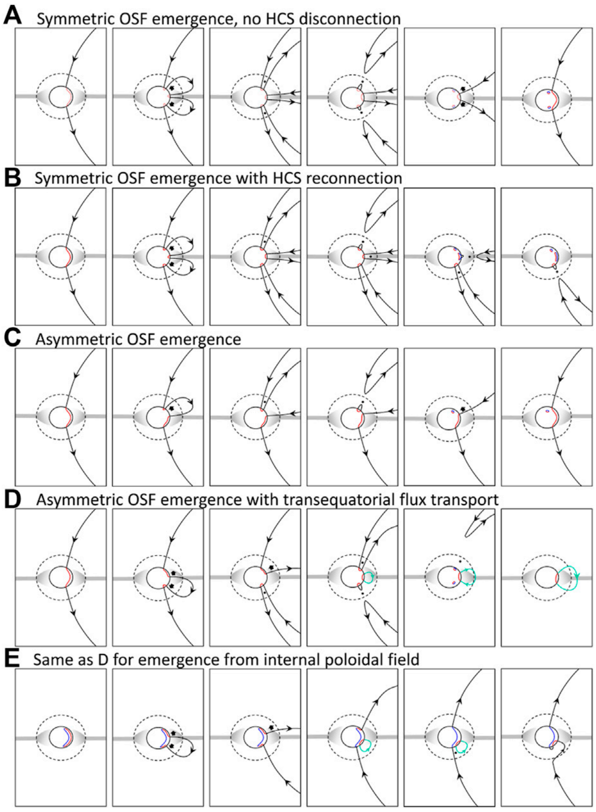

FIGURE 9
Topological sequences due to emergence, magnetic reconnection (in both the polar coronal holes and in the heliospheric current sheet, HCS), and transequatorial transfer of flux. All panels consider the situation after the polar fields have flipped and do not consider longitudinal structure which would allow different topologies to exist simultaneously at different longitudes. In panels **(A–D)** the poloidal field emerging is topologically connected to OSF in the heliosphere, and only **(E)** deals with emergence from poloidal field that remains in the sub-surface Sun. In each panel: the solid circle is the photosphere at $r = R_{\odot}$; the dashed circle is the source surface at $r = 2.5R_{\odot}$; the grey band is the HCS; and north is to the top. Red and blue lines are subsurface field line connectivities at $r < R_{\odot}$, with red/blue segments having a net poloidal component that is southward/northward. Black dots are reconnection sites, arrowed lines are magnetic field lines and block arrows give the poleward motion caused by meridional circulation. From top to bottom rows are for: **(A)** symmetric flux emergence in the two hemispheres without reconnection in the HCS; **(B)** symmetric emergence with reconnection between the lower-latitude leading-spot polarity fields in the HCS; **(C)** asymmetric emergence (in the northern hemisphere only), without transequatorial flux transport; **(D,E)** asymmetric emergence (in the southern hemisphere only) with transequatorial transport of the field of the leading-spot polarity. The difference between **(D,E)** is that in **(D)** the emergence is of magnetic field lines that near the poles thread the photosphere and coronal source surface and so form OSF, whereas in **(E)** the emergence is of internal poloidal field that never passes through the photosphere. The last 3 panels of sequences **(D,E)** also illustrate two ways in which closed field lines (shown in green) can make OSF migrate equatorward. In **(D)** the closed loop straddles the HCS (so was generated from two loops with HCS reconnection or from one loop with transequatorial transport) but does not emerge through the source surface (and become open) until the polar OSF is disconnected (termed mechanism 1 in the text). In **(E)** both photospheric footpoints of the loop are in the southern hemisphere and interchange reconnection of the OSF gives "footpoint jumping" to a lower latitude (termed mechanism 2 in the text). Note that the time differences between frames are not fixed and so different sequences take place over different timescales. Schematics based on those by Schrijver et al. (2002) and Lockwood et al. (2017).

Figure 8B shows detail of the modelled poleward magnetic flux surges in both hemispheres during solar cycle 19, as captured by the synthesized magnetogram: for the northern hemisphere the major ones are labelled $N_1$, $N_2$ and $N_3$ and for the southern they are $S_1$, $S_2$ and $S_3$. In this section, we look at the origins of these surges in terms of the various scenarios for the evolution of OSF topology illustrated schematically in Figure 9.

Figure 8B shows that the poleward surges in the northern hemisphere are related to the unusual behavior of the polar crown filament (PCF). Figure 6 illustrates how the poleward-most PCFs usually form late in solar cycles between the polar coronal hole, after it has flipped polarity, and the remnant, diffused field, predominantly of the leading-spot polarity, that is left at middle latitudes. At the start of the next cycle the latter is augmented by the trailing-polarity field of the next cycle and the divider between the two polarities becomes sharper and migrates poleward, carrying the next polar field reversal towards the pole. In the northern hemisphere during cycle 19, this evolution appears to have begun after the surge $N_1$, aided by surge $N_2$. The polar coronal hole of the new polarity ($B_r < 0$, in blue) was established by $N_1$ and a PCF formed at its equatorward edge and is enhanced by the surge of leading-spot polarity flux ($B_r > 0$, in green/yellow), $N_2$. However, instead of this boundary continuing to migrate toward the pole, its progress is interrupted by a major second poleward surge of negative $B_r$ field, $N_3$, and it is behind this surge that the PCF that brings the next polar field reversal to the pole forms. The corresponding sequence of surges is seen in the southern hemisphere but no clear and long-lived PCF was formed between surges $S_1$ and $S_2$ and only after surge $S_3$ does the main PCF clearly form and migrate poleward, which is much more typical behaviour.

The coloured histograms in the top and bottom panels of Figure 8 show the variations of polar fluxes ($F_{PN}$ and $F_{SN}$, in parts **A** and **C** respectively) deduced from the MWO observations of polar faculae. The black dots in **A** and **C** are 6-months averages of the polar field measured by the HSO magnetograph (from Babcock, 1959) and the mauve dots are 6-months averages of the polar field measured by the first magnetograph at Mount Wilson (MWO) (from Howard, 1972). In both cases the polar fields have been scaled to the polar cap fluxes $F_{PN}$ and $F_{PS}$ by multiplying by a constant area of $4 \times 10^{18} m^2$. These early magnetograph data have resolution and accuracy problems, and inspection of the early MWO data, in particular, reveals the resolution of the field measurements improving with time over the interval. Nevertheless they do show considerable agreement with the polar fluxes deduced from the faculae; however, there are also important and significant differences.

A key point to note is that the polar faculae measurements do not distinguish between toward field (radial component $B_r < 0$) and away field (radial component $B_r > 0$), whereas magnetograph data do and so both the two polarities of field average spatially (within pixels) and temporally (when data are averaged over time). In other words, polar faculae give $<|B_r|>$, whereas magnetograms give $<B_r>$. This offers an explanation of the interval of large difference between the northern polar flux from MWO images and from the early MWO magnetograph data for 1961–1963 shown in Figure 8A. This period also shows a difference between the flux deduced from polar faculae and the expectation of the modelling by Lockwood and Owens (2014). The implication is that within the surge $N_2$ there is considerable leading-spot polarity flux. The relatively good agreement between the magnetograph and polar facular data in the southern hemisphere shown in Figure 8C implies that this is not so true of the corresponding surge in the southern hemisphere, $S_2$. We conclude that the large excess of leading-spot polarity flux in the long-lived $N_2$ poleward surge adds to the polar cap flux which is the area integral of $|B_r|$ (and hence the polar flux deduced from MWO polar faculae observations) but reduces the polar field (and the flux that is the area integral of $B_r$) of the newly-reversed northern polar coronal hole. Over time, the opposite polarities reconnect and the polar flux deduced from faculae and magnetograph data converge again - also such that by the next solar minimum (at the end of cycle 19) it is the same as the flux for the southern hemisphere polar coronal hole, as shown in Figure 5B.

The surges are increases in transported flux, rather than meridional flow speed (although we do know that can, in general, vary) and all the photospheric surges in both hemispheres will carry magnetic flux taking part in one of the example topological sequences shown in Figure 9. In Figure 9A flux is emerging symmetrically in both hemispheres and there is no reconnection in the heliospheric current sheet nor any trans-equatorial transport of flux. This means that all emerged flux, of both the leading-spot and trailing-spot polarities, is eventually caught up in poleward meridional flow and moves toward the pole. Because the trailing spot polarity arrives first near the poles, this causes the polar coronal hole flux to firstly increase and then decrease and in the end there is no net effect on the polar cap flux. The sequence shown in row **B**, on the other hand, stops leading-spot polarity field reaching the polar cap by reconnecting it at the HCS (thereby disconnecting OSF that is lost down the HCS). For this case, after the polar field flip, this causes the OSF in both polar caps to decline. Row **C** shows asymmetric emergence of flux in the northern hemisphere, which we know occurred in the declining phase of cycle 19. Because there is not sufficient matching emerged flux in the southern hemisphere, both trailing-spot and then leading-spot polarity field reaches the pole and the sequences is as for part **A**, but only in the northern hemisphere. Row **D** shows what happens if asymmetrically-emerged flux migrates across the equator and so the two polarities of the loop become embedded in oppositely-directed meridional flow. The end result, in this case, is that the open flux in both polar caps is decreased. This point was made by Virtanen et al. (2018). The importance of transequatorial transfer in the evolution of the state of the solar magnetic field was stressed by Cameron et al. (2013) and Cameron et al. (2014). Some of this trans-equatorial transfer is caused by granular and supergranular motions giving a random walk of flux tubes, which can be treated as a diffusion process. However some transequatorial flux transport is due to systematic cross-equatorial flows such as those associated with the inflows into active regions, and some flux crosses the equator during the emergence process itself. In particular, a large sunspot group with a large tilt angle, can emerge close to the solar equator, particularly in the later phases of the sunspot cycle when heliographic latitudes of active regions are lower, and in relatively rare, but highly significant, events the emerged flux from the two polarities can appear in opposite hemispheres. These events, called “cross-equatorial flux plumes”, can contain sufficient flux that they make a very large difference to how the next sunspot cycle develops. The consequences of these sequences depends on the connectivity of the poloidal field that emerges. This is illustrated by comparison of parts **D** and **E** which are both for asymmetric emergence in the southern hemisphere with transequatorial transfer of the leading-spot polarity field into the northern hemisphere. The difference is that in **D** the field emerges from internal poloidal field that connects through the photosphere and coronal source surface to open flux whereas in **E** it emerges from internal poloidal field that does not thread the photosphere. It can be seen the consequences are different as **D** ends in reduced polar coronal flux in both hemispheres whereas **E** ends in increases polar coronal flux in both: however, note that the difference is only because there is prexisting opposite polarity polar OSF in **D** to cancel, whereas there is not in **E**.

The sequences shown in Figure 9 suggest that the asymmetric emergence of northern hemisphere open flux in cycle 19 did not necessarily build up an excess of signed coronal hole flux in the northern polar cap; however, because polar faculae arise from both polarities of field, they do all, at some stage, generate asymmetric peaks in numbers of polar faculae and unsigned polar coronal hole (if only briefly) (Deng et al., 2013). It is probable that these sequences have different implications for the poloidal subsurface field at the end of each cycle and, as this is the seed field for the next solar cycle, it is likely that there are remnant hemispheric asymmetries during the next cycle. It is noticeable in Figure 4 that sunspot emergence in the northern hemisphere continued to dominate in the rising phase of cycle 20. It is also interesting to note that the total unsigned polar flux (as measured by polar faculae) may be as important in determining the behaviour of the subsequent cycle as the total signed flux (Bhowmik, 2019). Often these two polar fluxes (the integrals of $|B_r|$ and $B_r$) are very similar in most cycles, but not in cycle 19 that is asymmetric in its hemispheric emergence pattern.

The initial poleward surges $N_1$ and $S_1$ in Figure 8 mainly contain trailing-spot polarity flux ($B_r < 0$, in blue, in $N_1$ and $B_r > 0$, in green/yellow, in $S_1$) that emerged early in the cycle and these cause the polar cap flips. The surges $N_2$ and $S_2$ will also contain some of this trailing-spot polarity field, but are dominated by leading-spot polarity flux. Surge $S_2$ occurs first and is consistent with the poleward motion of leading-spot polarity flux for an excess of emergence in the southern hemisphere. (Figure 5A shows that initially in cycle 19 there was a larger area of sunspots in the southern hemisphere). This is the kind of sequence shown in Figure 9C, but the excess flux emergence is in the southern hemisphere. Initially this sequence is contributing to the surge $S_1$ but then gives the surge $S_2$ the brings leading-spot polarity field to the pole (that is unable to reconnect across the HCS because of the lower emergence rate in the northern hemisphere), where it reconnects with the newly-formed southern polar coronal hole flux and so causes the reduction in $F_{PS}$ that is observed (seen in both the early magnetograph data and the polar faculae data).

Around the peak of cycle 19, the northern hemisphere starts to strongly dominate the flux emergence and the sequence shown in Figure 9C occurs - initially adding to the (negative) $F_{PN}$ before the strong and prolonged surge $N_2$ arrives, bringing the leading-spot polarity flux to the northern polar coronal hole. This reduces the magnitude of $F_{PN}$, as seen by a magnetograph but increases that seen in the polar faculae data. This is because this flux of leading-spot polarity field is so great it does not all immediately reconnect with the now established northern polar coronal hole flux this causes a rise in $F_{PN}$ as deduced from polar faculae because they do not discriminate between inward and outward polarity.

The synthesised magnetogram suggests that at the time labelled $T_E$ in Figure 8B there is trans-equatorial transfer of leading-spot polarity flux from the southern hemisphere ($B_r < 0$) into the northern hemisphere and this appears to give the poleward surges of trailing-spot polarity flux in both hemispheres, $N_3$ and $S_3$. These surges enhance and maintain the polar coronal holes and so we infer that they arise from purely internal magnetic field as in Figure 9E.

Hence the synthetic magnetogram appears to be consistent with the asymmetries in flux emergence shown by the sunspot data in Figure 5A, as well as the polar faculae, polar field and polar crown filament data. Note that the early dominance of southern hemisphere sunspot emergence is also consistent with the earlier flip of the southern hemisphere polar field, as seen in both polar faculae and the early HSO magnetograph data.

## 7.2 Changes in the spatial distribution of OSF over the sunspot cycle

There are two behaviours of open solar flux that are not captured by any of the main sequences in Figure 9 which consider only emergence of open flux in active regions and then poleward transfer to the polar coronal hole where it is lost by reconnection. The first of these is the formation of low-latitude extensions to polar coronal holes in the declining phase of each sunspot cycle (Bromage et al., 2000; Rouillard and Lockwood, 2007). The second is equatorward migration of coronal hole flux and OSF from both poles in the subsequent rising phase of the next cycle. The latter has been seen in studies using PFSS modelling (Wang and Sheeley, 1994; Bilenko and Tavastsherna, 2016; Huang et al., 2017) and also in studies of coronal hole distributions seen in infra-red maps and using full-disk magnetograms to determine the field polarity (Bilenko, 2002). This pole-to-pole migration takes place simultaneously for the two polarities at different longitudes. The field structure implied by the coronal holes varies from a dominant dipole field at sunspot minimum, almost parallel to the solar rotation axis, to a highly inclined dipole and higher-order multipole moments at sunspot maximum before the dominant dipole is re-established at the next solar minimum, but with the opposite polarity.

The meridional flow of photospheric field line footpoints remains poleward throughout. The second part of the pole-to-pole migrations of OSF of both polarities is at about the same time as, and is consistent with, the first poleward surge in a cycle of trailing-spot polarity flux in the photosphere. However, why and how in the first part of the pole-to-pole migration, OSF is moving equatorward while individual field line footpoints are propagating poleward is unclear. There seems to be only two possibilities: 1) closed flux tubes at lower latitudes become open by emerging through the coronal source in response to loss of polar OSF, giving an equatorward phase motion of OSF and/or 2) interchange reconnections with lower-latitude close loops cause footpoint-jumping to lower latitudes (Wang and Sheeley, 2004; Fisk and Zurbuchen, 2006).

Linker et al. (2011) argue that OSF at low latitudes produced by footpoint-jumping is rapidly lost by disconnection, making any isolated coronal hole formed short-lived: in which case, this is effectively just a different loss mechanism for polar coronal hole OSF. However, Owens et al. (2007) show how interchange reconnections via releases of coronal mass ejections could give pole-to-pole transfer of OSF of both polarities. These also can generate low-latitude extensions of polar coronal holes, without necessarily disconnecting any open flux at the poles or at the equatorial HCS. The sequence of events is illustrated in the last 3 frames of Figure 9E, where the closed field line loop is shown in green. If this operated in isolation, it and would mean OSF remained constant from one cycle to the next (i.e, there is perfect cycle-to-cycle OSF memory), which is not what is observed. However, if it this operated in conjunction with another mechanism it could provide some degree of memory from one cycle to the next, which is what is observed. Note that the latitudinal jumps caused by interchange reconnections need not be the large ones implied by CME releases, they could be small and of the type that allows the rigid rotation of low-latitude extensions of polar coronal holes despite the differential rotation of the underlying photosphere, as reviewed by Kahler and Hudson (2002) and as detected by Madjarska et al. (2004). In fact, the study of coronal holes by Bilenko (2002) suggests both small and large latitude jumps of flux tube footpoints occur, with the pole-to-pole transport starting with some coronal flux appearing in the opposite hemisphere (consistent with a CME release) and other polar coronal hole flux taking a small step equatorward in the same hemisphere (consistent with interchange reconnection with a small closed field line loop). Note that many small-loop jumps offer a potential explanation of steady slow solar wind along streamer belt OSF and the large footpoint jumps of transient CME events in the solar wind.

A mechanism of type 1) could also mean that OSF is, to some degree, conserved even if it is being disconnected at high latitudes. This explanation of the initial, equatorward, part of the inferred pole-to-pole migration of OSF is that closed flux in the corona moves up through the coronal source surface. This would be in response to loss of polar open flux (and consequent decrease in tangential magnetic pressure in the upper polar corona) caused by disconnection of polar OSF in the rising phase of the sunspot cycle. This suggestion is illustrated by the green field line loop in Figure 9D this would also give an equatorward migration of OSF in the rising phase of the sunspot cycle despite the poleward photospheric motion.

Both mechanism 1) and mechanism 2) offer an explanation of observations that the first surge to the pole in each cycle contains much more coronal hole flux than later surges (Fujiki et al., 2016; Hewins et al., 2020). Huang et al. (2017) show that the flux of OSF in the pole-to-pole transfer was larger after crossing the solar equator, presumably because trailing-spot polarity OSF is added by the emergence in active regions. This added OSF gave between 15 and 35% (in the 3 cycles studied) of the total OSF reaching the other pole. The idea that OSF arriving at the pole is a combination of OSF that has migrated from the other pole and newly added OSF is interesting as it gives some memory of the OSF from one sunspot cycle to the next but also some variability - both of which are clearly present in the cycle-to-cycle variation of OSF discussed in Paper 1 (Lockwood et al., 2022).

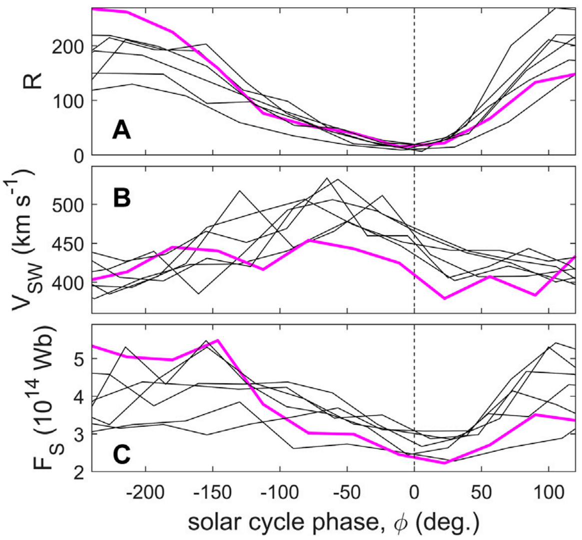

**FIGURE 10**
Variations with solar cycle phase $\phi$ of annual means of: **(A)** International Sunspot Number, R; **(B)** the solar wind speed, $V_{SW}$ derived from geomagnetic activity data; and **(C)** the open solar flux, $F_S$, again derived from geomagnetic data. The $V_{SW}$ and $F_S$ time series are shown in Figures 9 and 12 of Paper 1 (Lockwood et al., 2022). The phase $\phi$ is defined as zero at sunspot minimum and shown by the vertical dashed lines in each panel. The results are for sunspot cycles 17–24 around the MGSM peak, cycles for which the peak annual mean R exceeded 150. The variation for the sunspot minimum 19/20 is shown by the bold mauve line in all panels.

## 7.3 The variation of the average solar wind speed at low heliographic latitudes

There is another point about cycle 19 to consider and that is the variation in near-Earth solar wind speeds $V_{SW}$, reconstructed from geomagnetic activity. Figure 9 of Paper 1 shows that the peak in $V_{SW}$ during the declining phase of cycle 19 is considerably weaker and earlier than in most cycles. Those data are plotted here in a different format in Figure 10B, which shows the variation with solar cycle phase relative to sunspot minimum for the cycles around the peak of the MGSM. To compare cycles of comparable levels of solar activity we plot for the cycle minima at the start of cycles 17–21 which are the cycles for which the subsequent sunspot number maximum exceeded 150 (in annual means). The variation for cycle minimum 19/20 is shown by the bold mauve line.

The same feature was noted by Mursula et al. (2017) from different geomagnetic data and is also seen in the 27-days recurrence of geomagnetic activity caused by the fast streams emanating from the low-latitude coronal holes (see Lockwood et al., 1999). The considerably lower average $V_{SW}$ in the declining phase of cycle 19 and in the rising phase of cycle 20 is clear. The connection between fast solar wind streams at Earth and low-latitude coronal holes (e.g. Luhmann et al., 2002) means that this is evidence that low-latitude OSF was lower around the cycle minimum 19/20 than for the other cycles.

As noted above, the other notable feature of cycle 19 is that the OSF, $F_S$, derived from the geomagnetic data, was lower at its end than at its start despite the strong emergence of flux, indeed this cycle shows the highest sunspot number and area yet observed - and yet the OSF at the end of the cycle was lower that at the start. This can clearly be seen in part **C** of Figure 10 which shows the OSF falling from the highest solar maximum value at the maximum of cycle 19 to the lowest solar minimum value at and after the minimum 19/20. We deduce that the lower OSF value around the minimum 19/20 is, at least in part, a loss of low-latitude OSF which reduces the number and the speed of fast streams hitting Earth, thereby lowering the mean $V_{SW}$.

It is possible, maybe even probable, that this unusual loss of low-latitude OSF at the solar 19/20 minimum was linked to the unusual evolution of cycle 19 and the highly asymmetric hemispheric emergence of flux (and the consequent accumulation of OSF of both polarities in the northern polar coronal hole). Because the most marked drop in low-latitude $V_{SW}$ is towards the end of the declining phase of cycle 19 and before the start of flux emergence in cycle 20, this implies the drop in low-latitude OSF at this time is associated with a drop in pole-to-pole transfer of OSF rather than with a decline in the cycle of low-latitude flux emergence, poleward migration and loss at the poles. However, Figure 10C also shows that the subsequent growth of OSF in the rising phase of cycle 20 was also reduced.

We suggest that the initial drop in low-latitude OSF occurred because the surges $N_3$ and $S_3$, which finally established reasonably matched $F_{PN}$ and $F_{SN}$ (probably because of a significant transequatorial flux transfer event), resulted in fewer closed loops at lower latitudes. This could reduce the equatorward migration of OSF - be it by emergence of new OSF (mechanism 1) or interchange reconnections (mechanism 2). The implication is that it is the inferred pole-to-pole transfer of OSF that provides much of the cycle-to-cycle memory and this was disrupted in cycle 19 by the unusually asymmetric emergence pattern. Note this makes the cycle-to-cycle OSF memory somewhat different from the cycle-to-cycle memory of active region emergence which is more to do with the state of the poloidal seed field inside the Sun.

Looking at the variations around the MGSM, one of the most striking features that stands out is the hemispheric asymmetry in emergence during cycle 19 at the peak of the MGSM. In this section, we have considered some ways that this could have contributed to the breaking of "virtuous circle" (for OSF growth) that occurred over cycle 19. However, hemispheric asymmetry is not the only possibility - for example unusual latitudinal and tilt angle distributions of emergence may have been the key factor. This is closely intertwined with the issue of the relative importance of pole-to-pole OSF transfer and the cycle of OSF emergence, poleward transport and polar disconnection. These remain open questions. What is significant, however, is that holistic reconstruction techniques are beginning to throw some light on the processes that led to the rise, peak and fall of the MGSM. More understanding will be gained when the products of these reconstructions are used as input to the latest coronal modelling techniques. What is becoming increasingly evident as our understanding of past variation grows, however, is that transequatorial flux transfer and anti-Hale, or other rogue active region emergence are critical. Neither of these processes are predictable at the present time and they may never be so, and hence they are always likely to set limits to how predictable the amplitudes of solar activity cycles (particularly the second halves of cycles) can be.

## Author contributions

ML carried out the analysis and wrote the paper with text and figure contributions from all co-authors.

## Funding

This work is supported by a number of grants. ML, MO, and SY are supported by consolidated grant number *ST*/*M*000885/1 from the United Kingdom Science and Technology Facilities Council (UKRI/STFC) and ML and MO are also funded by the SWIGS Directed Highlight Topic Grant number *NE*/*P*016928/1/from the United Kingdom Natural Environment Research Council (UKRI/NERC). AY was supported by UKRI/STFC research grant number *ST*/*S*000321/1. IV was supported by the Academy of Finland *via* the ReSoLVE Centre of Excellence (project no. 307411). The work of IV and AY was also partially supported by the International Space Science Institute (Bern, Switzerland) via International Team 420 on Reconstructing Solar and Heliospheric Magnetic Field Evolution over the Past Century. The work of AM-J was funded by NASA Living with a Star grant *NNH*15*ZDA*001*N*.

## Acknowledgments

The authors are grateful to the funding bodies listed in the funding section and the great many scientists who contributed to compiling, preserving and distributing the many long-term historic datasets exploited in this paper and their funding organisations that enables them to do so. These are far to numerous to list here. Whilst being grateful to all these contributions, we also echo the comments of Pevtsov et al. (2019b) concerning the vital importance of funding to preserve and digitise historical monitoring data to enable us to bring all sources together to inform understanding of long-term variability of the Sun and space weather.

## Conflict of interest

The authors declare that the research was conducted in the absence of any commercial or financial relationships that could be construed as a potential conflict of interest.

## Publisher's note

## References

Abramenko, V., Yurchyshyn, V., Linker, J., Mikić, Z., Luhmann, J., and Lee, C. (2010). Low-latitude coronal holes at the minimum of the 23rd solar cycle. *Astrophys. J.* 712, 813–818. doi:10.1088/0004-637X/712/2/813

Altschuler, M. D., and Newkirk, G. (1969). Magnetic fields and the structure of the solar corona: I: Methods of calculating coronal fields. *Sol. Phys.* 9, 131–149. doi:10.1007/BF00145734

Arlt, R., Leussu, R., Giese, N., Mursula, K., and Usoskin, I. (2013). Sunspot positions and sizes for 1825–1867 from the observations by Samuel Heinrich Schwabe. *Mon. Not. R. Astron. Soc.* 433, 3165–3172. doi:10.1093/mnras/stt961

Arlt, R., Senthamizh Pavai, V., Schmiel, C., and Spada, F. (2016). Sunspot positions, areas, and group tilt angles for 1611-1631 from observations by christoph scheiner. *Astron. Astrophys.* 595, A104. doi:10.1051/0004-6361/201629000

Arlt, R. (2014). Sunspots from the past, treasures for today. *Astronomy Geophys.* 55, 3.24–3.27. doi:10.1093/astrogeo/atu125

Babcock, H., and Babcock, H. (1952). Mapping the magnetic fields of the sun. *Publicat. Astron. Soc. Pacific*, 64, 282–287. doi:10.1086/126495

Babcock, H. (1953). The solar magnetograph. *Astrophys. J.* 118, 387–396. doi:10.1086/145767

Babcock, H. (1959). The Sun's polar magnetic field. *Astrophys. J.* 130, 364–365. doi:10.1086/146726

Babcock, H. W. (1961). The topology of the Sun's magnetic field and the 22-year cycle. *Astrophys. J.* 133, 572–587. doi:10.1086/147060

Belík, M., Marková, E., and Druckmüller, M. (2006). Structural changes in solar corona during total solar eclipses. *Proc. Int. Astron. Union* 2, 251–252. doi:10.1017/S1743921306001955

Bhowmik, P. (2019). Polar flux imbalance at the sunspot cycle minimum governs hemispheric asymmetry in the following cycle. *Astron. Astrophys.* 632, A117. doi:10.1051/0004-6361/201834425

Bhowmik, P., and Yeates, A. (2022). Two classes of eruptive events during solar minimum. *Sol. Phys.* 296, 109. doi:10.1007/s11207-021-01845-x

Bigelow, F. (1890). Further study of the solar corona. *Am. J. Sci.* 40, 343–358. doi:10.2475/ajs.s3-40.239.343

Bilenko, I. (2002). Coronal holes and the solar polar field reversal. *Astron. Astrophys.* 396, 657–666. doi:10.1051/0004-6361:20021412

Bilenko, I., and Tavastsherna, K. (2016). Coronal hole and solar global magnetic field evolution in 1976 – 2012. *Sol. Phys.* 291, 2329–2352. doi:10.1007/s11207-016-0966-2

Boe, B., Habbal, S., and Druckmüller, M. (2020). Coronal magnetic field topology from total solar eclipse observations. *Astrophys. J.* 895, 123. doi:10.3847/1538-4357/ab8ae6

Bromage, B., Alexander, D., Breen, A., Clegg, J., Del Zanna, G., DeForest, C., et al. (2000). Structure of a large low-latitude coronal hole. *Sol. Phys.* 193, 181–193. doi:10.1023/A:1005209725885

Cameron, R. H., Dasi-Espuig, M., Jiang, J., Işık, E., Schmitt, D., and Schüssler, M. (2013). Limits to solar cycle predictability: Cross-equatorial flux plumes. *Astron. Astrophys.* 557, A141. doi:10.1051/0004-6361/201321981

Cameron, R., Jiang, J., Schmitt, D., and Schüssler, M. (2010). Surface flux transport modeling for solar cycles 15-21: Effects of cycle-dependent tilt angles of sunspot groups. *Astrophys. J.* 719, 264–270. doi:10.1088/0004-637X/719/1/264

Cameron, R., Jiang, J., Schüssler, M., and Gizon, L. (2014). Physical causes of solar cycle amplitude variability. *J. Geophys. Res. Space Phys.* 119, 680–688. doi:10.1002/2013JA019498

Carrasco, V., Vaquero, J., Gallego, M., Muñoz-Jaramillo, A., de Toma, G., Galaviz, P., et al. (2019). Sunspot characteristics at the onset of the maunder minimum based on the observations of Hevelius. *Astrophys. J.* 886, 18. doi:10.3847/1538-4357/ab4ade

Chatzistergos, T., Ermolli, I., Krivova, N., Solanki, S., Banerjee, D., Barata, T., et al. (2020). Analysis of full-disc Ca II K spectroheliograms: III. Plage area composite series covering 1892–2019. *Astron. Astrophys.* 639, A88. doi:10.1051/0004-6361/202037746

Cliver, E. (2014). The extended cycle of solar activity and the Sun's 22-year magnetic cycle. *Space Sci. Rev.* 186, 169–189. doi:10.1007/s11214-014-0093-z

Cranmer, S. R. (2009). Coronal holes. *Living Rev. Sol. Phys.* 6, 3. doi:10.12942/lrsp-2009-3

Das, R., Ghosh, A., and Karak, B. (2022). Is the hemispheric asymmetry of sunspot cycle caused by an irregular process with long-term memory? *Mon. Not. R. Astron. Soc.* 511, 472–479. doi:10.1093/mnras/stac035

Dasi-Espuig, M., Jiang, J., Krivova, N., Solanki, S., Unruh, Y., and Yeo, K. (2016). Reconstruction of spectral solar irradiance since 1700 from simulated magnetograms. *Astron. Astrophys.* 590, A63. doi:10.1051/0004-6361/201527993

Dasi-Espuig, M., Solanki, S., Krivova, N., Cameron, R., and Peñuela, T. (2010). Sunspot group tilt angles and the strength of the solar cycle. *Astron. Astrophys.* 518, A7. doi:10.1051/0004-6361/201014301

Davis, C., Bell, S., Stamper, R., Poole, A., McKinnell, L., and Wilkinson, P. (2009). A potential lag between the open solar magnetic source flux and solar EUV and X-ray emissions as measured by the Earth's ionosphere during total solar eclipses. *Ann. Geophys.* 27, 2449–2456. doi:10.5194/angeo-27-2449-2009

Davis, C., Clarke, E., Bamford, R., Lockwood, M., and Bell, S. (2001). Long term changes in EUV and X-ray emissions from the solar corona and chromosphere as measured by the response of the Earth's ionosphere during total solar eclipses from 1932 to 1999. *Ann. Geophys.* 19, 263–273. doi:10.5194/angeo-19-263-2001

Davis, C., Lockwood, M., Bell, S., Smith, J., and Clarke, E. (2000). Ionospheric measurements of relative coronal brightness during the total solar eclipses of 11 August, 1999 and 9 July, 1945. *Ann. Geophys.* 18, 182–190. doi:10.1007/s00585-000-0182-z

Deng, L., Qu, Z., Liu, T., and Huang, W. (2013). The hemispheric asynchrony of polar faculae during solar cycles 19–22. *Adv. Space Res.* 51, 87–95. doi:10.1016/j.asr.2012.08.013

Diercke, A., and Denker, C. (2019). Chromospheric synoptic maps of polar crown filaments. *Sol. Phys.* 294, 152. doi:10.1007/s11207-019-1538-z

Dikpati, M., and Charbonneau, P. (1999). A babcock-leighton flux transport dynamo with solar-like differential rotation. *Astrophys. J.* 518, 508–520. doi:10.1086/307269

Druckmüller, M., Rušin, V., and Milan, M. (2006). A new numerical method of total solar eclipse photography processing. *Contrib. Astron. Obs. Skaln. Pleso* 36, 131–148.

Dyson, F. (1927). Ix. Drawings of the corona from photographs at total eclipses from 1896 to 1922. *Philosophical Trans. R. Soc. Lond. Ser. A* 226, 363–388. doi:10.1098/rsta.1927.0009

Emery, B. A., Webb, D. F., Gibson, S. E., Hewins, I. M., McFadden, R. H., and Kuchar, T. A. (2021). Latitude variations in primary and secondary polar crown polarity inversion lines and polar coronal hole boundaries over five solar cycles. *Sol. Phys.* 296, 119. doi:10.1007/s11207-021-01857-7

Fisk, L., and Zurbuchen, T. (2006). Distribution and properties of open magnetic flux outside of coronal holes. *J. Geophys. Res.* 111, A09115. doi:10.1029/2005JA011575

Fujiki, K., Tokumaru, M., Hayashi, K., Satonaka, D., and Hakamada, K. (2016). Long-term trend of solar coronal hole distribution from 1975 to 2014. *Astrophys. J.* 827, L41. doi:10.3847/2041-8205/827/2/L41

Goelzer, M., Smith, C., Schwadron, N., and McCracken, K. (2013). An analysis of heliospheric magnetic field flux based on sunspot number from 1749 to today and prediction for the coming solar minimum. *J. Geophys. Res. Space Phys.* 118, 7525–7531. doi:10.1002/2013JA019404

Gold, T. (1955). The symmetry of the corona of 1954 june 30. *Mon. Notices R. Astronomical Soc.* 115, 340–342. doi:10.1093/mnras/115.4.340

Gurgenashvili, E., Zaqarashvili, T., Kukhianidze, V., Oliver, R., Ballester, J., Dikpati, M., et al. (2017). North–south asymmetry in rieger-type periodicity during solar cycles 19–23. *Astrophys. J.* 845, 137. doi:10.3847/1538-4357/aa830a

Habbal, S., and Druckmüller, M. (2019). Hiding the sun: Coronal discoveries during total solar eclipses. *Sci. (Bristol).* doi:10.33548/SCIENTIA422

Hale, G., Ellerman, F., Nicholson, S., and Joy, A. (1919). The magnetic polarity of sun-spots. *Astrophys. J.* 49, 153–186. doi:10.1086/142452

Hale, G. (1908). Solar vortices (contributions from the Mt. Wilson solar observatory, no. 26). *Astrophys. J.* 28, 100. doi:10.1086/141581

Hanaoka, Y., Nakazawa, J., Ohgoe, O., Sakai, Y., and Shiota, K. (2014). Coronal mass ejections observed at the total solar eclipse on 13 november 2012. *Sol. Phys.* 289, 2587–2599. doi:10.1007/s11207-014-0476-z

Hathaway, D., and Upton, L. (2016). Predicting the amplitude and hemispheric asymmetry of solar cycle 25 with surface flux transport. *JGR. Space Phys.* 121 (10744–10), 753. doi:10.1002/2016JA023190

Hayakawa, H., Lockwood, M., Owens, M. J., Sôma, M., Besser, B. P., and van Driel-Gesztelyi, L. (2021). Graphical evidence for the solar coronal structure during the maunder minimum: Comparative study of the total eclipse drawings in 1706 and 1715. *J. Space Weather Space Clim.* 11, 1. doi:10.1051/swsc/2020035

Hazra, G., and Choudhuri, A. (2019). A new formula for predicting solar cycles. *Astrophys. J.* 880, 113. doi:10.3847/1538-4357/ab2718

Hazra, S., Brun, A., and Nandy, D. (2020). Does the mean-field α effect have any impact on the memory of the solar cycle? *Astron. Astrophys.* 642, A51. doi:10.1051/0004-6361/201937287

Hewins, I., Gibson, S., Webb, D., McFadden, R., Kuchar, T., Emery, B., et al. (2020). The evolution of coronal holes over three solar cycles using the McIntosh archive. *Sol. Phys.* 295, 161. doi:10.1007/s11207-020-01731-y

Howard, R. (1972). Polar magnetic fields of the sun: 1960-1971. *Sol. Phys.* 25, 5–13. doi:10.1007/BF00155740

Huang, G.-H., Lin, C.-H., and Lee, L. C. (2017). Solar open flux migration from Pole to Pole: Magnetic field reversal. *Sci. Rep.* 7, 9488.1–9488.7. doi:10.1038/s41598-017-09862-2

Hyder, C. (1965). The ”polar crown” of filaments and the Sun’s polar magnetic fields. *Astrophys. J.* 141, 272. doi:10.1086/148108

Jørgensen, C., Karoff, C., Pavai, V., and Arlt, R. (2019). Christian Horrebow’s sunspot observations – I. Life and published writings. *Sol. Phys.* 294, 77. doi:10.1007/s11207-019-1465-z

Judge, P. G., Burkepile, J., de Toma, G., and Druckmüller, M. (2010). “Historical eclipses and the recent solar minimum corona,” in *SOHO-23: Understanding a peculiar solar minimum*. Editors S. Cranmer, J. Hoeksema, and J. Kohl (San Francisco: Astronomical Society of the Pacific), Vol. 428, 171–176. doi:10.48550/arXiv.1001.5278

Koskela, J., Virtanen, I., and Mursula, K. (2019). Revisiting the coronal current sheet model: Parameter range analysis and comparison with the potential field model. *Astron. Astrophys.* 631, A17. doi:10.1051/0004-6361/201935967

Kahler, S., and Hudson, H. (2002). Boundary structures and changes in long-lived coronal holes. *Astrophys. J.* 574, 467–476. doi:10.1086/340937

Karoff, C., Jørgensen, C., Senthamizh Pavai, V., and Arlt, R. (2019). Christian Horrebow’s sunspot observations – II. Construction of a record of sunspot positions. *Sol. Phys.* 294, 78. doi:10.1007/s11207-019-1466-y

Krivova, N., Solanki, S. K., Hofer, B., Wu, C.-J., Usoskin, I. G., and Cameron, R. (2021). Modelling the evolution of the Sun’s open and total magnetic flux. *Astron. Astrophys.* 650, A70. doi:10.1051/0004-6361/202140504

Lamy, P., Barlyaeva, T., Llebaria, A., and Floyd, O. (2014). Comparing the solar minima of cycles 22/23 and 23/24: The view from LASCO white light coronal images. *J. Geophys. Res. Space Phys.* 119, 47–58. doi:10.1002/2013JA019468

Lebecq, C., Koutchmy, S., and Stellmacher, G. (1985). The 1981 total solar eclipse corona. II. Global absolute photometric analysis. *Astronomy Astrophysics* 152, 157–164.

Leighton, R. (1964). Transport of magnetic fields on the sun. *Astrophys. J.* 140, 1547–1562. doi:10.1086/148058

Leussu, R., Usoskin, I., Arlt, R., and Mursula, K. (2016). Properties of sunspot cycles and hemispheric wings since the 19th century. *Astron. Astrophys.* 592, A160. doi:10.1051/0004-6361/201628335

Levine, R. (1982). Open magnetic fields and the solar cycle: I: Photospheric sources of open magnetic flux. *Sol. Phys.* 79, 203–230. doi:10.1007/BF00146241

Li, J. (2018). A systematic study of Hale and anti-hale sunspot physical parameters. *Astrophys. J.* 867, 89–16. doi:10.3847/1538-4357/aae31a

Li, K., Irie, M., Wang, J., Xiong, S., Yun, H., Liang, H., et al. (2002). Activity cycle of polar faculae. *Publicat. Astron. Soc. Japan*, 54, 787–792. doi:10.1093/pasj/54.5.787

Li, K., Yun, H., and Gu, X. (2001). Hemispheric variation in solar activity. *Astrophys. J.* 554, L115–L117. doi:10.1086/320914

Lin, H., Kuhn, J., and Coulter, R. (2004). Coronal magnetic field measurements. *Astrophys. J.* 613, L177–L180. doi:10.1086/425217

Linker, J. A., Heinemann, S., Temmer, M., Owens, M., Caplan, R. M., Arge, C., et al. (2021). Coronal hole detection and open magnetic flux. *Astrophys. J.* 918, 21.1–21.18. doi:10.3847/1538-4357/ac090a

Linker, J., Lionello, R., Mikić, Z., Titov, V., and Antiochos, S. (2011). The evolution of open magnetic flux driven by photospheric dynamics. *Astrophys. J.* 731, 110.1–110.11. doi:10.1088/0004-637X/731/2/110

Lockwood, M., and Owens, M. (2021). *Astronomy Geophys.* 62, 3.12–3.19. doi:10.1093/astrogeo/atab065Cosmic meteorology

Lockwood, M., Owens, M., Barnard, L., Davis, C., and Steinhilber, F. (2011). The persistence of solar activity indicators and the descent of the Sun into Maunder Minimum conditions. *Geophys. Res. Lett.* 38, L22105. doi:10.1029/2011GL049811

Lockwood, M., Owens, M., Barnard, L., Scott, C., Frost, A., Yu, B., et al. (2022). Application of historic datasets to understanding open solar flux and the 20th-century grand solar maximum. 1. geomagnetic, ionospheric and sunspot observations. *Front. Astronomy Space Phys.* doi:10.3389/fspas.2022.960775

Lockwood, M., and Owens, M. (2014). Centennial variations in sunspot number, open solar flux and streamer belt width: 3. Modeling. *J. Geophys. Res. Space Phys.* 119, 5193–5209. doi:10.1002/2014JA019973

Lockwood, M., Owens, M., Imber, S., James, M., Bunce, E., and Yeoman, T. (2017). Coronal and heliospheric magnetic flux circulation and its relation to open solar flux evolution. *JGR. Space Phys.* 122, 5870–5894. doi:10.1002/2016JA023644

Lockwood, M., Stamper, R., and Wild, M. N. (1999). A doubling of the Sun’s coronal magnetic field during the past 100 years. *Nature* 399, 437–439. doi:10.1038/20867

Lockwood, M. (2003). Twenty-three cycles of changing open solar magnetic flux. *J. Geophys. Res.* 108, 1128. doi:10.1029/2002JA009431

Loucif, M. L., and Koutchmy, S. (1989). Solar cycle variations of coronal structures. *Astronomy Astrophysics Suppl. Ser.* 77, 45–66. ADS Bibcode: 1989A&AS. . .77. . .45L.

Low, B. (1991). Three-dimensional structures of magnetostatic atmospheres. III - a general formulation. *Astrophys. J.* 370, 427–434. doi:10.1086/169829

Luhmann, J., Li, Y., Arge, C., Gazis, P., and Ulrich, R. (2002). Solar cycle changes in coronal holes and space weather cycles: Solar wind sources. *J. Geophys. Res.* 107, SMP 3-1–SMP 3-12. doi:10.1029/2001JA007550

Mackay, D. H. (2021). “Solar prominences,” in *Oxford research encyclopedia of physics* (Oxford, United Kingdom: Oxford University Press), 1–27. doi:10.1093/acrefore/9780190871994.013.17

Mackay, D., and Yeates, A. (2012). The Sun’s global photospheric and coronal magnetic fields: Observations and models. *Living Rev. Sol. Phys.* 9, 6. doi:10.12942/lrsp-2012-6

Madjarska, M., Doyle, J., and van Driel-Gesztelyi, L. (2004). Evidence of magnetic reconnection along coronal hole boundaries. *Astrophys. J.* 603, L57–L59. doi:10.1086/383030

Makarov, V., Tlatov, A., Callebaut, D., Obridko, V., and Shelting, B. (2001). Large-scale magnetic field and sunspot cycles. *Sol. Phys.* 198, 409–421. doi:10.1023/A:1005249531228

Makarov, V., Tlatov, A., and Callebaut, D. (2003). Polar faculae and sunspot cycles concerning secular variation of polar magnetic flux. *Astron. Nachr.* 324, 381. doi:10.1002/asna.200310136

Mandal, S., Krivova, N., Solanki, S., Sinha, N., and Banerjee, D. (2020). Sunspot area catalog revisited: Daily cross-calibrated areas since 1874. *Astron. Astrophys.* 640, A78. doi:10.1051/0004-6361/202037547

Marzouk, B., Stoeva, P., and Stoev, A. (2016). White light coronal structures and flattening during six total solar eclipses. *NRIAG J. Astronomy Geophys.* 5, 297–300. doi:10.1016/j.nrjag.2016.08.003

McClintock, B., Norton, A., and Li, J. (2014). Re-examining sunspot tilt angle to include anti-Hale statistics. *Astrophys. J.* 797, 130.1–130.10. doi:10.1088/0004-637X/797/2/130

McIntosh, P. (1972). Solar magnetic fields derived from hydrogen alpha filtergrams. *Rev. Geophys.* 10, 837–856. doi:10.1029/RG010i003p00837

Mikić, Z., Downs, C., Linker, J., Caplan, R., Mackay, D., Upton, L., et al. (2018). Predicting the corona for the 21 August 2017 total solar eclipse. *Nat. Astron.* 2, 913–921. doi:10.1038/s41550-018-0562-5

Minnis, C. (1956). Interpretation of ionospheric measurements made during solar eclipses. *Nature* 178, 33–34. doi:10.1038/178033b0

Mordvinov, A., Karak, B., Banerjee, D., Chatterjee, S., Golubeva, E., and Khlystova, A. (2020). Long-term evolution of the Sun's magnetic field during cycles 15–19 based on their proxies from kodaikanal solar observatory. *Astrophys. J.* 902, L15. doi:10.3847/2041-8213/abba80

Mordvinov, A., Karak, B., Banerjee, D., Golubeva, E., Khlystova, A., Zhukova, A., et al. (2021). Evolution of the Sun's activity and the poleward transport of remnant magnetic flux in Cycles 21–24. *Mon. Not. R. Astron. Soc.* 510, 1331–1339. doi:10.1093/mnras/stab3528

Mordvinov, A. V., and Kitchatinov, L. L. (2019). Evolution of the Sun's polar fields and the poleward transport of remnant magnetic flux. *Sol. Phys.* 294, 21.1–21.14. doi:10.1007/s11207-019-1410-1

Muñoz-Jaramillo, A., Dasi-Espuig, M., Balmaceda, L., and DeLuca, E. (2013). Solar cycle propagation, memory, and prediction: Insights from a century of magnetic proxies. *Astrophys. J.* 767, L25. doi:10.1088/2041-8205/767/2/L25

Muñoz-Jaramillo, A., Navarrete, B., and Campusano, L. (2021). Solar anti-hale bipolar magnetic regions: A distinct population with systematic properties. *Astrophys. J.* 920, 31. doi:10.3847/1538-4357/ac133b

Muñoz-Jaramillo, A., Sheeley, N., Zhang, J., and DeLuca, E. (2012). Calibrating 100 years of polar faculae measurements: Implications for the evolution of the heliospheric magnetic field. *Astrophys. J.* 753, 146. doi:10.1088/0004-637X/753/2/146

Mursula, K., Holappa, L., and Lukianova, R. (2017). Seasonal solar wind speeds for the last 100 years: Unique coronal hole structures during the peak and demise of the grand modern maximum. *Geophys. Res. Lett.* 44, 30–36. doi:10.1002/2016GL071573

Nagy, M., Lemerle, A., and Charbonneau, P. (2019). Impact of rogue active regions on hemispheric asymmetry. *Adv. Space Res.* 63, 1425–1433. doi:10.1016/j.asr.2018.12.018

Nagy, M., Lemerle, A., Labonville, F., Petrovay, K., and Charbonneau, P. (2017). The effect of "rogue" active regions on the solar cycle. *Sol. Phys.* 292, 167. doi:10.1007/s11207-017-1194-0

Nepomnyashchikh, A., Mandal, S., Banerjee, D., and Kitchatinov, L. (2019). Can the long-term hemispheric asymmetry of solar activity result from fluctuations in dynamo parameters? *Astron. Astrophys.* 625, A37. doi:10.1051/0004-6361/201935224

Okunev, O., and Kneer, F. (2004). On the structure of polar faculae on the sun. *Astron. Astrophys.* 425, 321–331. doi:10.1051/0004-6361:20041120

Owens, M., and Crooker, N. (2006). Coronal mass ejections and magnetic flux buildup in the heliosphere. *J. Geophys. Res.* 111, A10104. doi:10.1029/2006JA011641

Owens, M., and Crooker, N. (2007). Reconciling the electron counterstreaming and dropout occurrence rates with the heliospheric flux budget. *J. Geophys. Res.* 112, A06106. doi:10.1029/2006JA012159

Owens, M. J., Crooker, N. U., and Lockwood, M. (2011). How is open solar magnetic flux lost over the solar cycle? *J. Geophys. Res.* 116, A04111. doi:10.1029/2010JA016039

Owens, M. J., and Lockwood, M. (2012). Cyclic loss of open solar flux since 1868: The link to heliospheric current sheet tilt and implications for the maunder minimum. *J. Geophys. Res.* 117, A04102. doi:10.1029/2011JA017193

Owens, M. J., Lockwood, M., and Riley, P. (2017a). Global solar wind variations over the last four centuries. *Sci. Rep.* 7, 41548. doi:10.1038/srep41548

Owens, M., Schwadron, N., Crooker, N., Hughes, W., and Spence, H. (2007). Role of coronal mass ejections in the heliospheric Hale cycle. *Geophys. Res. Lett.* 34, L06104. doi:10.1029/2006GL028795

Parker, E. (1955). Hydromagnetic dynamo models. *Astrophys. J.* 122, 293–314. doi:10.1086/146087

Pasachoff, J. M., Rušin, V., Druckmüller, M., Aniol, P., Saniga, M., and Minarovjech, M. (2009). The 2008 august 1 eclipse solar-minimum corona unravelled. *Astrophys. J.* 702, 1297–1308. doi:10.1088/0004-637X/702/2/1297

Petrie, G., and Haislmaier, K. (2013). Low-latitude coronal holes, decaying active regions, and global coronal magnetic structure. *Astrophys. J.* 775, 100.1–100.14. doi:10.1088/0004-637X/775/2/100

Petrovay, K., and Nagy, M. (2018). Rogue active regions and the inherent unpredictability of the solar dynamo. *Proc. Int. Astron. Union* 13, 307–312. doi:10.1017/S1743921318001254

Petrovay, K. (2020). Solar cycle prediction. *Living Rev. Sol. Phys.* 17, 2. doi:10.1007/s41116-020-0022-z

Pevtsov, A. A., Tlatova, K. A., Pevtsov, A. A., Heikkinen, E., Virtanen, I., Karachik, N. V., et al. (2019a). Reconstructing solar magnetic fields from historical observations: V. Sunspot magnetic field measurements at Mount wilson observatory. *Astron. Astrophys.* 628, A103. doi:10.1051/0004-6361/201834985

Pevtsov, A., Griffin, E., Grindlay, J., Kafka, S., Bartlett, J., Usoskin, I., et al. (2019b). Historical astronomical data: Urgent need for preservation, digitization enabling scientific exploration. *arXiv preprint*. Publisher: arXiv Version Number: 1. doi:10.48550/ARXIV.1903.04839

Pevtsov, A., Virtanen, I., Mursula, K., Tlatov, A., and Bertello, L. (2016). Reconstructing solar magnetic fields from historical observations: I. Renormalized Ca K spectroheliograms and pseudo-magnetograms. *Astron. Astrophys.* 585, A40. doi:10.1051/0004-6361/201526620

Pishkalo, M. (2011). Flattening index of the solar corona and the solar cycle. *Sol. Phys.* 270, 347–363. doi:10.1007/s11207-011-9749-y

Pontin, D. I., and Priest, E. R. (2022). Magnetic reconnection: MHD theory and modelling. *Living Rev. Sol. Phys.* 19, 1. doi:10.1007/s41116-022-00032-9

Priyal, M., Banerjee, D., Karak, B., Muñoz-Jaramillo, A., Ravindra, B., Choudhuri, A. R., et al. (2014). Polar network index as a magnetic proxy for the solar cycle studies. *Astrophys. J.* 793, L4. doi:10.1088/2041-8205/793/1/L4

Priyatikanto, R. (2016). Shape parameters of the solar corona from 1991 to 2016. *Res. Astron. Astrophys.* 16, 181–187. doi:10.1088/1674-4527/16/12/181

Ranyard, A. (1879). Photographs and drawings of the corona. *Memoirs R. Astron. Soc.* 41, 483–768.

Ranyard, A. (1871). The corona. *Nature* 4, 466. doi:10.1038/004466e0

Raouafi, N., Riley, P., Gibson, S., Fineschi, S., and Solanki, S. (2016). Diagnostics of coronal magnetic fields through the hanle effect in UV and IR lines. *Front. Astron. Space Sci.* 3. doi:10.3389/fspas.2016.00020

Reginald, N., Gopalswamy, N., Yashiro, S., Gong, Q., and Guhathakurta, M. (2017). Replacing the polarizer wheel with a polarization camera to increase the temporal resolution and reduce the overall complexity of a solar coronagraph. *J. Astron. Telesc. Instrum. Syst.* 3, 014001. doi:10.1117/1.JATIS.3.1.014001

Rice, O., and Yeates, A. (2021). Global coronal equilibria with solar wind outflow. *Astrophys. J.* 923, 57. doi:10.3847/1538-4357/ac2c71

Riley, P., Linker, J., and Mikić, Z. (2001). An empirically-driven global MHD model of the solar corona and inner heliosphere. *J. Geophys. Res.* 106, 15889–15901. doi:10.1029/2000JA000121

Riley, P., Lionello, R., Linker, J., Mikic, Z., Luhmann, J., and Wijaya, J. (2011). Global MHD modeling of the solar corona and inner heliosphere for the whole heliosphere interval. *Sol. Phys.* 274, 361–377. doi:10.1007/s11207-010-9698-x

Rouillard, A., and Lockwood, M. (2007). The latitudinal effect of corotating interaction regions on galactic cosmic rays. *Sol. Phys.* 245, 191–206. doi:10.1007/s11207-007-9019-1

Rušin, V., Druckmüller, M., Aniol, P., Minarovjech, M., Saniga, M., Mikić, Z., et al. (2010). Comparing eclipse observations of the 2008 August 1 solar corona with an MHD model prediction. *Astron. Astrophys.* 513, A45. doi:10.1051/0004-6361/200912778

Rušin, V. (2000). "Shape and structure of the white-light corona over solar cycles," in *Last total solar eclipse of the millennium*. Editors W. W. Livingston and A. Özgüç (San Francisco: Astronomical Society of the Pacific), Vol. 205, 171–176. doi:10.48550/arXiv.1001.5278

Rušin, V. (2017). The flattening index of the eclipse white-light corona and magnetic fields. *Sol. Phys.* 292, 24.1–24.9. doi:10.1007/s11207-016-1046-3

Saez, F., Zhukov, A., Lamy, P., and Llebaria, A. (2005). On the 3-dimensional structure of the streamer belt of the solar corona. *Astron. Astrophys.* 442, 351–358. doi:10.1051/0004-6361:20042016

Schatten, K. H., Wilcox, J. M., and Ness, N. F. (1969). A model of interplanetary and coronal magnetic fields. *Sol. Phys.* 6, 442–455. doi:10.1007/BF00146478

Schrijver, C., DeRosa, M., and Title, A. (2002). What is missing from our understanding of long-term solar and heliospheric activity? *Astrophys. J.* 577, 1006–1012. doi:10.1086/342247

Schüssler, M., and Cameron, R. H. (2018). Origin of the hemispheric asymmetry of solar activity. *Astron. Astrophys.* 618, A89. doi:10.1051/0004-6361/201833532

Schwadron, N., Connick, D., and Smith, C. (2010). Magnetic flux balance in the heliosphere. *Astrophys. J.* 722, L132–L136. doi:10.1088/2041-8205/722/2/L132

Seaton, D., De Groof, A., Shearer, P., Berghmans, D., and Nicula, B. (2013). Swap observations of the long-term, large-scale evolution of the extreme-ultraviolet solar corona. *Astrophys. J.* 777, 72–14. doi:10.1088/0004-637X/777/1/72

Sheeley, N., Jr. (1991). Polar faculae - 1906-1990. *Astrophys. J.* 374, 386–389. doi:10.1086/170129

Simon, P. (1979). Polar coronal holes and solar cycles. *Sol. Phys.* 63, 399–410. doi:10.1007/BF00174544

Sivaraman, K. R. (2000). Results from Kodaikanal synoptic observations. *J. Astrophys. Astron.* 21, 149–153. doi:10.1007/BF02702380

Solanki, S., Schüssler, M., and Fligge, M. (2000). Evolution of the Sun's large-scale magnetic field since the Maunder minimum. *Nature* 408, 445–447. doi:10.1038/35044027

Sturrock, P. A., and Smith, S. M. (1968). Magnetic-field structure associated with coronal streamers. *Sol. Phys.* 5, 87–101. doi:10.1007/BF00147122

Sun, X., Hoeksema, J., Liu, Y., and Zhao, J. (2015). On polar magnetic field reversal and surface flux transport during solar cycle 24. *Astrophys. J.* 798, 114.1–114.8. doi:10.1088/0004-637X/798/2/114

Sýkora, J., Badalyan, O., and Obridko, V. (2003). Connections between the white-light eclipse corona and magnetic fields over the solar cycle. *Sol. Phys.* 212, 301–318. doi:10.1023/A:1022933619413

Sýkora, J., Badalyan, O., and Obridko, V. (2002). Relationship between the coronal shape and the magnetic field topology during the solar cycle. *Adv. Space Res.* 29, 395–400. doi:10.1016/S0273-1177(01)00602-0

Thomas, S., Owens, M., and Lockwood, M. (2014). The 22-year Hale cycle in cosmic ray flux – evidence for direct heliospheric modulation. *Sol. Phys.* 289, 407–421. doi:10.1007/s11207-013-0341-5

Tlatov, A. G. (2010). The centenary variations in the solar corona shape in accordance with the observations during the minimal activity epoch. *Astron. Astrophys.* 522, A27. doi:10.1051/0004-6361/201014082

Tlatov, A., and Tlatova, K. (2020). Polar and low-latitude faculae in activity cycles 23–24. *Geomagn. Aeron.* 60, 825–830. doi:10.1134/S0016793220070245

Vaquero, J. M., and Vázquez, M. (2009). *The Sun recorded through history: Scientific data extracted from historical documents*. vol. 361 of Astrophysics and Space Science Library. New York, NY: Springer. doi:10.1007/978-0-387-92790-9

Vieira, E. A., and Solanki, S. K. (2010). Evolution of the solar magnetic flux on time scales of years to millenia. *Astron. Astrophys.* 509, A100. doi:10.1051/0004-6361/200913276

Virtanen, I., and Mursula, K. (2019). Photospheric and coronal magnetic fields in six magnetographs: III. Photospheric and coronal magnetic fields in 1974–2017. *Astron. Astrophys.* 626, A67. doi:10.1051/0004-6361/201935713

Virtanen, I., and Mursula, K. (2016). Photospheric and coronal magnetic fields in six magnetographs: I. Consistent evolution of the bashful ballerina. *Astron. Astrophys.* 591, A78. doi:10.1051/0004-6361/201628096

Virtanen, I., and Mursula, K. (2017). Photospheric and coronal magnetic fields in six magnetographs: II. Harmonic scaling of field intensities. *Astron. Astrophys.* 604, A7. doi:10.1051/0004-6361/201730863

Virtanen, I. O. I., Pevtsov, A. A., Virtanen, I. I., and Mursula, K. (2021). Reconstructing solar magnetic fields from historical observations: VII. Far-Side activity in surface flux transport simulations. *Astron. Astrophys.* 652, A79. doi:10.1051/0004-6361/202140656

Virtanen, I. O. I., Virtanen, I. I., Pevtsov, A. A., Bertello, L., Yeates, A., and Mursula, K. (2019a). Reconstructing solar magnetic fields from historical observations: IV. Testing the reconstruction method. *Astron. Astrophys.* 627, A11. doi:10.1051/0004-6361/201935606

Virtanen, I., Virtanen, I., Pevtsov, A., and Mursula, K. (2018). Reconstructing solar magnetic fields from historical observations: III. Activity in one hemisphere is sufficient to cause polar field reversals in both hemispheres. *Astron. Astrophys.* 616, A134. doi:10.1051/0004-6361/201732323

Virtanen, I., Virtanen, I., Pevtsov, A., and Mursula, K. (2019b). Reconstructing solar magnetic fields from historical observations: Vi. axial dipole moments of solar active regions in cycles 21-24. *Astron. Astrophys.* 632, A39. doi:10.1051/0004-6361/201936134

Virtanen, I., Virtanen, I., Pevtsov, A., Yeates, A., and Mursula, K. (2017). Reconstructing solar magnetic fields from historical observations: II. Testing the surface flux transport model. *Astron. Astrophys.* 604, A8. doi:10.1051/0004-6361/201730415

Vokhmyanin, M., Arlt, R., and Zolotova, N. (2020). Sunspot positions and areas from observations by Thomas Harriot. *Sol. Phys.* 295, 39. doi:10.1007/s11207-020-01604-4

Vokhmyanin, M. V., and Zolotova, N. (2018). Sunspot positions and areas from observations by Galileo Galilei. *Sol. Phys.* 293, 31. doi:10.1007/s11207-018-1245-1

Waldmeier, M. (1966). Die totale sonnenfinsternis vom 30. mai 1965. *Naturwissenschaften* 53, 423–428. doi:10.1007/BF00654503

Waldmeier, M. (1955). Ergebnisse der zurcher sonnenfinsternisexpedition 1954. *Z. Astrophys.* 36, 275–292.

Waldmeier, M. (1977). Predicted and observed coronal structure. *Nature* 265, 611. doi:10.1038/265611a0

Waldmeier, M. (1971). The asymmetry of solar activity in the years 1959-1969. *Sol. Phys.* 20, 332–344. doi:10.1007/BF00159763

Wallace, S., Arge, C. N., Pattichis, M., Hock-Mysliwiec, R. A., and Henney, C. J. (2019). Estimating total open heliospheric magnetic flux. *Sol. Phys.* 294, 19. doi:10.1007/s11207-019-1402-1

Wang, Y.-M., and Lean, J. (2021). A new reconstruction of the Sun's magnetic field and total irradiance since 1700. *Astrophys. J.* 920, 100. doi:10.3847/1538-4357/ac1740

Wang, Y.-M., Robbrecht, E., Rouillard, A., Sheeley, N., and Thernisien, A. (2010). Formation and evolution of coronal holes following the emergence of active regions. *Astrophys. J.* 715, 39–50. doi:10.1088/0004-637X/715/1/39

Wang, Y.-M., and Sheeley, N. (1994). Global evolution of interplanetary sector structure, coronal holes, and solar wind streams during 1976-1993: Stackplot displays based on solar magnetic observations. *J. Geophys. Res.* 99, 6597. doi:10.1029/93JA02105

Wang, Y.-M., and Sheeley, N. R., Jr. (1992). On potential field models of the solar corona. *Astrophys. J.* 392, 310. doi:10.1086/171430

Wang, Y.-M., Sheeley, N., Socker, D., Howard, R., and Rich, N. (2000). The dynamical nature of coronal streamers. *J. Geophys. Res.* 105, 25133–25142. doi:10.1029/2000JA000149

Wang, Y.-M. (2017). Surface flux transport and the evolution of the Sun's polar fields. *Space Sci. Rev.* 210, 351–365. doi:10.1007/s11214-016-0257-0

Wang, Y., Biersteker, J., Sheeley, N., Jr., Koutchmy, S., Mouette, J., and Druckmuller, M. (2007). The solar eclipse of 2006 and the origin of raylike features in the white-light corona. *Astrophys. J.* 660, 882–892. doi:10.1086/512480

Wang, Y., and Sheeley, N., Jr. (2004). Footpoint switching and the evolution of coronal holes. *Astrophys. J.* 612, 1196–1205. doi:10.1086/422711

Wang, Y., Sheeley, N., Jr., Howard, R., Kraemer, J., Rich, N., Andrews, M., et al. (1997). Origin and evolution of coronal streamer structure during the 1996 minimum activity phase. *Astrophys. J.* 485, 875–889. doi:10.1086/304467

Webb, D., Gibson, S., Hewins, I., McFadden, R., Emery, B., Malanushenko, A., et al. (2018). Global solar magnetic field evolution over 4 solar cycles: Use of the McIntosh archive. *Front. Astron. Space Sci.* 5, 23. doi:10.3389/fspas.2018.00023

Wiegelmann, T., and Sakurai, T. (2021). Solar force-free magnetic fields. *Living Rev. Sol. Phys.* 18, 1. doi:10.1007/s41116-020-00027-4

Wiegelmann, T., Thalmann, J., and Solanki, S. (2014). The magnetic field in the solar atmosphere. *Astron. Astrophys. Rev.* 22, 78. doi:10.1007/s00159-014-0078-7

Wolf, R. (1852). Neue untersuchungen über die periode der sonnenflecken und ihre bedeutung (New investigations regarding the period of sunspots and its significance). *Mittheilungen der Naturforschenden Gesellschaft Bern* 255, 249–270.

Xu, Y., Banerjee, D., Chatterjee, S., Pötzi, W., Wang, Z., Ruan, X., et al. (2021). Migration of solar polar crown filaments in the past 100 years. *Astrophys. J.* 909, 86. doi:10.3847/1538-4357/abdc1e

Xu, Y., Pötzi, W., Zhang, H., Huang, N., Jing, J., and Wang, H. (2018). Collective study of polar crown filaments in the past four solar cycles. *Astrophys. J.* 862, L23. doi:10.3847/2041-8213/aad40d

Yeates, A., Baker, D., and van Driel-Gesztelyi, L. (2015). Source of a prominent poleward surge during solar cycle 24. *Sol. Phys.* 290, 3189–3201. doi:10.1007/s11207-015-0660-9

Yeates, A. (2020). How good is the bipolar approximation of active regions for surface flux transport? *Sol. Phys.* 295, 119. doi:10.1007/s11207-020-01688-y

Yeates, A., Mackay, D., van Ballegooijen, A., and Constable, J. (2010). A nonpotential model for the Sun's open magnetic flux. *J. Geophys. Res.* 115, A09112. doi:10.1029/2010JA015611